

ATLAS Electromagnetic Calorimeter Photon Trigger Efficiency Measurements and Improvements

Theodore Hirt Madden
University of Southampton
Final Report

June 27, 2025

Trigger systems used within ATLAS are key for precision measurements, testing the standard model and searches for beyond standard model physics. Triggers make fast decisions, accepting or rejecting detected objects, reducing a 40MHz bunch crossing rate to a 1kHz particle information storage rate. This paper measures, and explores improvements to, the level-1 trigger efficiencies using the Tag and Probe method on Z boson decays with final state radiation, $Z \rightarrow e^+e^-\gamma$. A new isolation parameter optimisation algorithm is proposed and tested using a Monte Carlo cross validation method. The new algorithm showed a 1.8% average efficiency increase in the 90% efficiency region of the 15GeV threshold trigger with the same total background rejection, compared to the Medium isolation trigger. Performance measurements showed the Medium isolation, single photon, 25 GeV threshold trigger reached at least 90% at 28 GeV. The Loose isolation, diphoton, 22 GeV single cluster threshold trigger reached 90% efficiency at ~ 25 GeV and $> 97\%$ efficiency at 35GeV. The Medium isolation, diphoton, 15 GeV single cluster threshold trigger reached 90% efficiency at ~ 19 GeV, rising to 95% at ~ 22 GeV and comparison to it's unisolated trigger counterpart showed a prominent efficiency decrease around 90% efficiency. Measurement of the offline photon transverse momenta at 90% trigger efficiency with respect to isolation and cluster energy threshold showed a non-linear decrease in the selection efficiency below 18 GeV. Triggers showed good efficiency uniformity with pseudorapidity and pileup.

Contents

1	Introduction	3
1.1	The ATLAS Detector	3
1.2	The ATLAS Electromagnetic Calorimeter	4
1.3	The ATLAS Trigger System	4
1.4	Particle Showers	5
1.5	Photons in ATLAS	6
1.6	Electron Feature Extractor Algorithms	6
1.6.1	Trigger Isolation	6
1.6.2	New 2025 Isolation Parameter - RHadV2	8
1.7	Tag and Probe Method	8
1.8	Event Selection	8
1.8.1	Photon Trigger Matching	9
1.8.2	Monte Carlo Dataset Event Selection	9
2	ATLAS Photon Trigger Performance Measurements	10
2.1	Trigger Efficiencies	10
2.1.1	Efficiency Statistics	10
2.1.2	New Efficiency Curve Fitting Method	10
2.1.3	Trigger Performance Measurements	11
2.2	Results	12
2.2.1	Sample Purity	12
2.2.2	Efficiency Curves	12
2.2.3	Pseudo rapidity Trigger Performance	13
2.2.4	Pileup Trigger Performance	13
2.2.5	Trigger Isolation Threshold Performance	14
3	Trigger Isolation Tuning Algorithm	16
3.1	Trigger Isolation Tuning	16
3.2	Summed Volume Tables	17
3.3	Implementing New Level 1 Trigger Tuning Algorithm	19
3.3.1	Rate Calculations	19
3.4	Monte Carlo Cross Validation	20
3.5	Results	20
3.5.1	Isolation Correlation	20
3.5.2	Isolation Tune Performance Measurement	21
3.5.3	Isolation Tuning Performance Cross Validation	23
3.5.4	Isolation Tuning Parameter Cross Validation	24
3.5.5	New Algorithm Efficiency Curve	26
4	Discussion	27
4.1	Efficiency Performance Measurements	27
4.2	Isolation Tuning Algorithm	28
5	Conclusion	29

1 Introduction

The Large Hadron Collider (LHC) at CERN collides protons at $\sqrt{s} = 13$ TeV to test the standard model (SM), make precise measurements of particle properties and search for physics beyond the standard model (BSM). Prompt photons are a key aspect of this work, being one of the main decay channels used in discovery and measurement of the Higgs boson[1, 2]. The LHC currently runs with an average pileup of 60 interactions per bunch crossing[3] and could push to up to 200 interactions per bunch crossing[4] for phase 2 operations. Accurate identification of photons, in the increasingly challenging running conditions, is fundamental to allow the advancement of particle physics through these precise measurements.

The ATLAS collaboration has previously published numerous papers on trigger performance measurement. In 2012, the Tag and Probe method using $Z \rightarrow e^+e^-\gamma$ events was introduced[5] using $\sqrt{s} = 8$ TeV ATLAS data. Two main papers cover the 2015-2018 data taking period, with ref. [6] making a cut on the dilepton invariant mass to select final state radiation (FSR) photons and remove coincident initial state radiation(ISR) photons. Ref. [7] made performance measurements on photons at the beginning of the LHC run 3, after the long shutdown. This paper uses $Z \rightarrow e^+e^-\gamma$ decays from 12fb^{-1} of $\sqrt{s} = 13$ TeV ATLAS data delivered since October 2024, re-simulated to include the new 2025 level-1(L1) trigger isolation definition. This report presents 2025 photon trigger performance measurements for key kinematic variables: pileup (μ), pseudorapidity (η) and photon transverse momenta (p_t). Previously, L1 isolation tuning focussed on electrons using $Z \rightarrow ee$ decays. This report uses a data driven approach to test a photon optimised L1 trigger, tuning trigger isolation, on photons, at trigger energy thresholds used to seed photon trigger chains and analysis, for improved L1 photon trigger efficiencies. A new tuning algorithm is implemented for calculating optimal isolation thresholds for use in L1 triggers, Monte Carlo cross validation (MCCV) is used to test the new tuning algorithm and performance comparisons are made to the current Medium trigger isolation.

The paper first describes the ATLAS detector, calorimeter and trigger system in sections 1.1 to 1.3. Sections 1.4 and 1.5 discuss detection within a calorimeter and the use of photons within ATLAS analysis. Section 1.6 introduces and describes the concept of energy clusters, trigger isolation, and the isolation variables used within the ATLAS L1 trigger. Section 1.7 outlines the Tag and Probe method used in the event selection. Section 1.8 presents the full event selection, photon matching to calorimeter clusters and truth matching to Monte Carlo event generated photons. Section 2 describes efficiency and proposes a new efficiency curve fitting method for measuring ATLAS photon trigger performance with respect to p_t , η , μ and trigger calorimeter cluster energy threshold ($E_{\text{Threshold}}$). Section 3 introduces the firmware implementation of the ATLAS isolation variables and their tuning. Then summed volume tables (SVT) are introduced and shown to be applicable to isolation parameter tuning. A new tuning algorithm is presented and tested with MCCV, comparing to the current Medium trigger isolation. Section 4 Discusses the results of the trigger performance measurements and application of the new isolation tuning algorithm.

1.1 The ATLAS Detector

The ATLAS detector[8, 3] is a general purpose particle detector covering the full range of η and ϕ . The detector measures particles produced in high energy proton-proton collisions and was designed for tests of beyond standard model physics, including, originally, the search for the Higgs boson[1].

The detector uses a right handed coordinate system. The azimuthal angle ϕ is measured around the beam pipe, the polar angle θ is measured relative to the beam axis. For electrons and photons the pseudo-rapidity is defined $\eta = -\ln \tan \frac{\theta}{2}$. Transverse momenta measures momenta perpendicular to the beam axis[8].

Fig.1a shows a cut away view of the detector. The detector consists of 4 main parts. The inner detector is immersed in a 2T magnetic field and deals with precise measurements of the interaction vertices, tracks and particle momenta measurements. The electromagnetic(EM) calorimeter uses liquid argon (LAr) technology, covering the range $|\eta| < 3.2$, the forward calorimeter (FCal) covers up to $|\eta| < 4.9$. The EM calorimeter is designed to completely absorb all the energy from electromagnetic particles such as electrons, positrons and photons, giving precise information on their energy and location. The hadronic calorimeter surrounds the EM calorimeter and uses LAr technology in the range $1.5 < |\eta| < 4.9$. Scintillator-tile calorimeters are used in the range $|\eta| < 1.7$. The muon spectrometers surround the calorimeters, detecting charged particles that exit the EM and hadronic calorimeters.

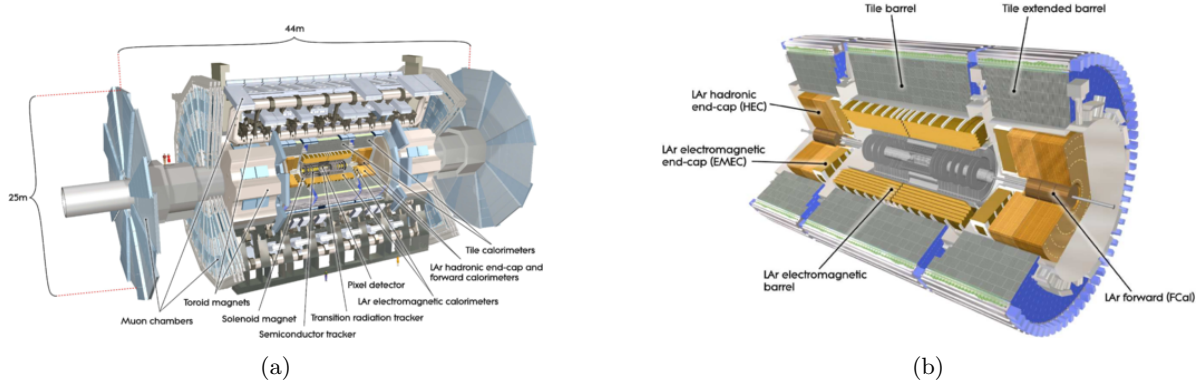


Figure 1: (a) A cut-away view of the ATLAS detector labelling the detector components[8] (b) A diagram of the liquid argon calorimeter in the ATLAS detector[9]

1.2 The ATLAS Electromagnetic Calorimeter

The EM calorimeter is split into the barrel ($|\eta| < 1.475$), inner end-cap ($1.375 < |\eta| < 2.5$) and outer end-cap ($2.5 < |\eta| < 3.2$) regions. The region $|\eta| < 1.8$ has a thin pre sampler attached to make energy corrections for losses before the object hits the calorimeter[9]. The ATLAS calorimeters are made up of a high density absorbing medium that stops incoming particles and an active medium which measures the energy of the incoming particles[3]. The EM calorimeter consists of liquid argon with an accordion geometry, which gives full azimuthal coverage due to overlapping layers of detector material. The region between the barrel and end cap is called the transition region. The substantial amount of material in front of the first calorimeter layer[10], and the differing geometries between the barrel and end cap can cause difficulties in reconstruction within the transition region.

The EM barrel calorimeter contains 4 layers[9]. The pre-sampler has elementary detecting cells of size $\Delta\eta \times \Delta\phi = 0.025 \times 0.1$. The front layer has cells of size $\Delta\eta \times \Delta\phi = 0.003125 \times 0.1$. The middle layer has cells of size $\Delta\eta \times \Delta\phi = 0.025 \times 0.025$. The back layer has cells of size $\Delta\eta \times \Delta\phi = 0.05 \times 0.025$. Cell information in the calorimeter cannot be individually used due to bandwidth and computational limitations. As such, a collection of cells have their energy summed over. Before phase I, the calorimeter was divided into "trigger towers" which summed all the layers' energies in regions of size $\Delta\eta \times \Delta\phi = 0.1 \times 0.1$. The phase I upgrade introduced the concept of Super Cells which provide information from each layer and improved the resolution of the front and middle layers to $\Delta\eta \times \Delta\phi = 0.025 \times 0.1$ [11]. The segmentation allows a finer energy resolution on the detected particles and allows the implementation of shower shape algorithms (see Section 1.6.1) in the level 1 trigger for improved electron and photon identification[11]. Fig.2 shows diagrams of the legacy trigger tower and new super cell configurations of the electronics within the calorimeter alongside a plot of the energy resolution comparison between the two configurations.

1.3 The ATLAS Trigger System

The ATLAS data acquisition and storage systems cannot handle the $40MHz$ bunch crossing rate occurring in the detector during data taking. To mitigate this ATLAS implements a multi level trigger system that functions in a hierarchical fashion. Each level builds on the decisions of the previous one, making increasingly refined decisions on whether to reject or retain detected objects, with the option to apply additional selection criteria if needed. Events are recorded that meet the criteria of a trigger chain. The set of trigger chains used during a run constitutes a trigger menu[12]. The trigger is implemented to minimise the rate of recorded events however it must efficiently collect an unbiased sample of useful physics processes[7]. The trigger system is split into two levels.

The Level-1 (L1) Trigger implements a hardware based system that makes rapid decisions in under $2.5\mu s$ on reduced-granularity calorimeter energy data using custom programmable FPGAs. It aims to efficiently select high transverse momenta events significant to physics analyses whilst rejecting background and noise based processes. The L1 trigger identifies regions of interest (RoIs), localised clusters of energy within the calorimeter identifying an area that contains an object likely to pass the criteria for storage to disk. RoIs are passed to the High Level Trigger (HLT) at a rate of $\approx 100kHz$ down from the

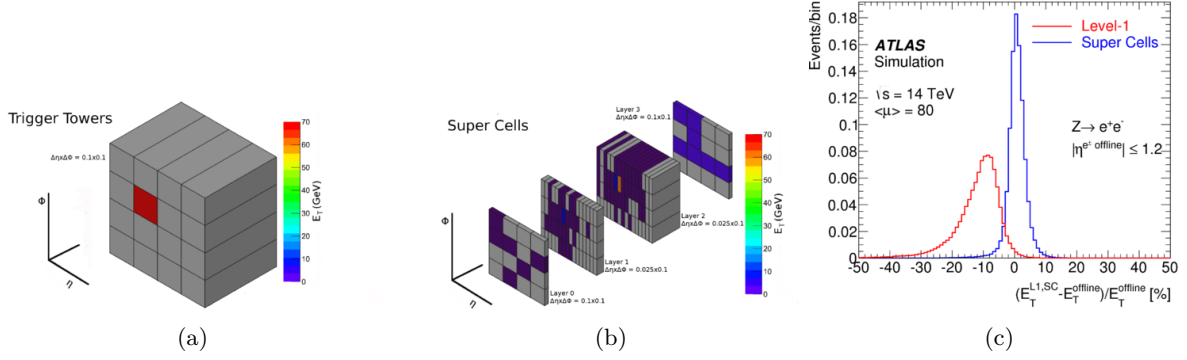


Figure 2: (a) A diagram of the legacy trigger towers showing how an EM object appears to the electronics (b) A diagram of the upgraded Super Cell configuration showing how an EM object looks to the upgraded electronics (c) The percentage difference in energy between L1 cluster energy($E_T^{L1,SC}$) and offline reconstructed electron transverse energy($E_T^{offline}$) using simulated $Z \rightarrow e^+e^-$ events. The legacy trigger towers curve is shown in red. The upgraded Super Cell curve is shown in blue showing a much tighter distribution in energy[11]

40MHz bunch crossing rate[6].

The High Level Trigger is a software based trigger that makes use of the full detector information. The HLT uses information not available at Level 1 including fine granularity calorimeter information, measurement from the muon spectrometer, muon trigger decision and tracking information from the inner detector. The HLT can perform more sophisticated algorithms such as track fitting[13], machine learning likelihood techniques and particle flow algorithms[14] to improve particle identification. The HLT reduces the rate from $\approx 100kHz$ to $\approx 1kHz$ for storage to disk.

1.4 Particle Showers

Shower shapes form from the interaction of an incident particle with the medium of the calorimeter[15, 16]. Only the electromagnetic and strong interactions are used in calorimetry, the other interactions are too weak. High energy Electromagnetic showers form from three main interactions: pair production, bremsstrahlung and Compton scattering. Lower energy photons are usually absorbed via the photoelectric effect.

Calorimeters have an inherent energy resolution[17, 18] ΔE , which depends upon it's energy E ,

$$\frac{\Delta E}{E} = \frac{a}{\sqrt{E}} \oplus \frac{b}{E} \oplus c \equiv \sqrt{\frac{a^2}{E} + \frac{b^2}{E^2} + c^2} \quad (1)$$

The energy resolution depends upon a stochastic term a , measuring statistical fluctuations in shower detection. b accounts for electronic noise and particles from other collision events, c depends on the specific calorimeter and does not decrease with energy. For ATLAS, $a = 0.1\text{GeV}^{\frac{1}{2}}$, $b = 0.17\text{GeV}$ and $c = 0.007$ [17].

Calorimeters also make use of a characteristic radiation length, X_0 , characterising the rate of electron energy loss due to bremsstrahlung[15]. The ATLAS EM calorimeters have a radiation length of approx. 1.8cm . Electromagnetic showers have a roughly 1% leakage for calorimeters with a radiation length of approx. $25X_0$ and ATLAS has calorimeters of approx. $45\text{cm}(25X_0)$ thickness. Lateral shower width is parametrised by the Molière radius[16] and Monte-Carlo simulations have shown that approx. 90% of an EM shower's energy is contained within this radius. The ATLAS EM calorimeter second and third layers were segmented based on the Molière radius[19]. The original trigger towers at a size of $\Delta\eta \times \Delta\phi = 0.1 \times 0.1$ were designed slightly larger than the Molière radius(0.08 in η)[20]. These expected observables, alongside the geometry of the detector are used to improve identification of EM objects.

1.5 Photons in ATLAS

Photons can be generated directly from decays, such as the decay of the Higgs boson to two photons[2], or they can come from final state radiation such as radiative Z boson decays. The final state radiation photons give access to a much lower p_t phase space. This is useful in testing the low energy threshold L1 triggers. Fig. 3 shows the difference in the transverse momenta distribution between reconstructed photons and electrons for the sample of particles chosen using the event selection described in section 1.8.

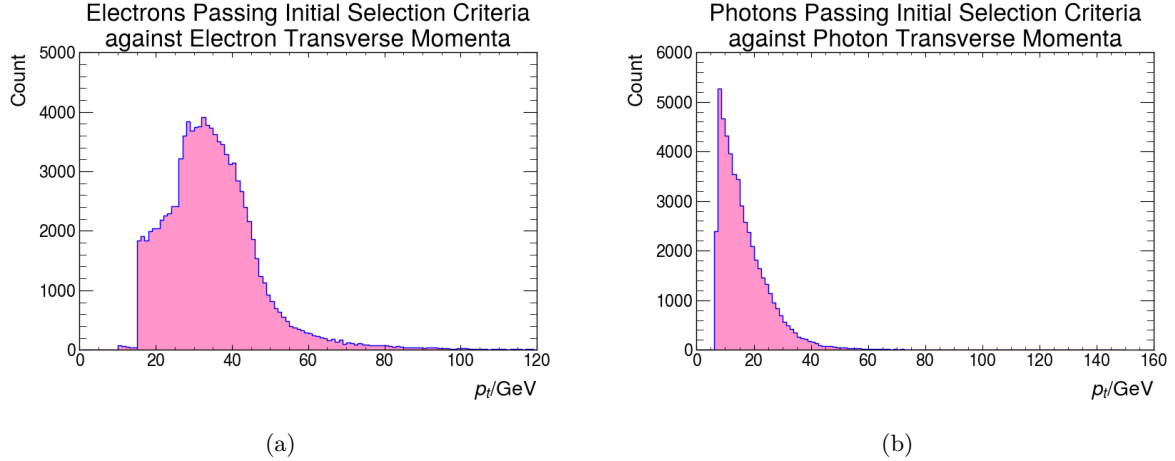


Figure 3: (a) Distribution of reconstructed electron transverse momenta(p_t) showing a peak at approx. 42GeV (b) Distribution of reconstructed photon transverse momenta showing a peak at approx. 10GeV

The currently used L1 triggers in photon trigger chains are: eEM26M which has a calorimeter cluster energy threshold of 25GeV and Medium isolation requirements, 2eEM24L which is a diphoton trigger, has a cluster energy threshold of 22GeV and loose isolation requirements and 2eEM18M which is a diphoton trigger, has a threshold of 15GeV and Medium isolation requirements. Photons and electrons are not primarily distinguished at L1 hence these L1 triggers, especially eEM26M, are also used for electron trigger chains. The eEM26M trigger is used to measure beyond standard model physics with $p_t > 140\text{GeV}$ photons, for precise measurements of the Higgs mass[21, 22], and for detected HLT photon-tau pairs with $p_t > 25\text{GeV}$. The 2eEM24L trigger measures HLT photon pairs with one photon above 35GeV and the other above 25GeV . The 2eEM18M trigger is used for HLT photon pairs with p_t of 20GeV and 22GeV . The trigger is used in searches for beyond standard model physics such as light particles decaying to two photons[23, 24].

1.6 Electron Feature Extractor Algorithms

The electron feature extractor(eFex) system[7] contains 24 modules with four algorithm processing FPGAs and one control FPGA. Trigger towers in the new system are made up of 10 Super Cells, shown in fig. 4a. Each FPGA processes the data of 32 trigger towers covering a total area of $\Delta\eta \times \Delta\phi = 0.4 \times 0.8$ per FPGA. Input data for each tower to the FPGA includes information on the surrounding trigger towers spanning an area $\Delta\eta \times \Delta\phi = 0.3 \times 0.3$. The module searches for energy clusters within the EM calorimeter. The energy cluster algorithm searches for a local energy maxima within the second layer of the calorimeter using a sliding window algorithm. 4 Super Cells from the second layer of a trigger tower are compared looking for the highest energy deposit and this is called the 'seed'. The cluster directionality in ϕ is computed by finding the highest energy Super Cell adjacent(in ϕ) to the seed. A cluster is then formed from a 3×2 grid of Super Cells directed in the calculated ϕ direction centred on the seed. Fig. 4b shows a diagram of this process. Cluster energy is then calculated by summing the total energy across the 4 layers within the 3×2 Super Cell block centred on the seed Super Cell. This corresponds to summing a 1×2 Super Cell block in the pre-sampler and third layer, and a 3×2 block in the first and second layer.

1.6.1 Trigger Isolation

The definition of isolation with respect to trigger isolation is different to the standard definition of isolation within a detector. The trigger isolation is defined with respect to the spread of the energy

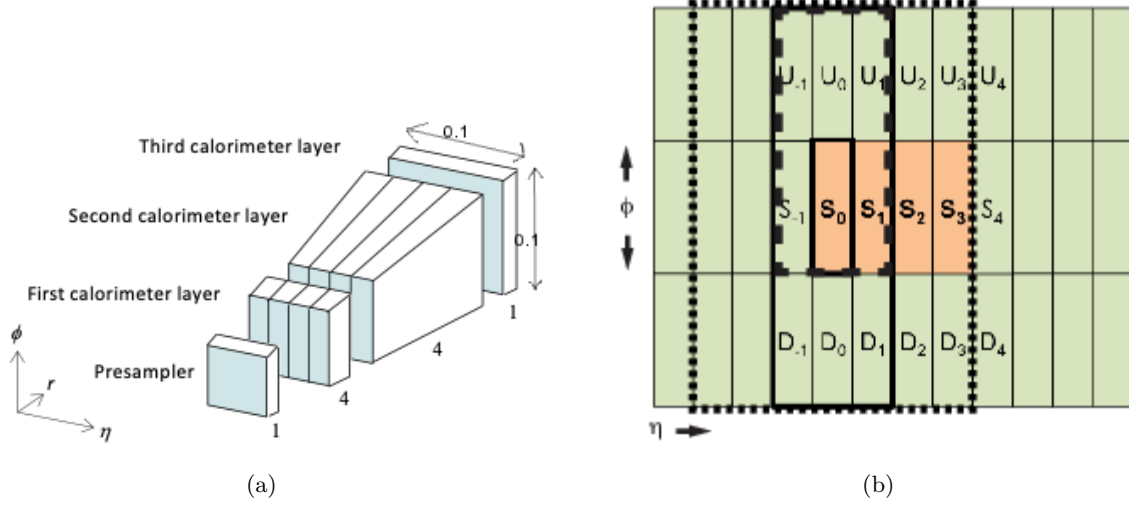


Figure 4: (a) A diagram of the Super Cells that make up a trigger tower, a trigger tower is now made up of 10 Super Cells (b) A diagram of the L1Calo seed finder algorithm. The S letters show the possible seeds in the second layer of the calorimeter, the U and D letters represent the directionality by finding the largest energy deposit adjacent to the seed. The solid rectangle shows the 3×3 block of Super Cells surrounding the maximum energy seed S_0 . The dashed rectangle shows the 3×2 block of Super Cells defining the cluster with 'upward' directionality U_0 . The dotted rectangle shows the 7×3 block of Super Cells used as the environment in calculation of shower width[3].

cluster within the calorimeter.

The eFex modules employ coarse-grain isolation algorithms to reduce the event rate and improve background rejection[3]. These algorithms are designed based on the expected shower shape development within the calorimeter (see Section 1.4) and are collectively referred to as isolation. In L1 trigger isolation, three shower shape algorithms are used: R_{Eta} , R_{Had} and W_{STot} .

The R_{Eta} algorithm computes the shower width measuring the ratio of the cluster energy to the energy of the surrounding environment.

$$R_{Eta} = 1 - \frac{E_{cluster}}{E_{environment}} \quad (2)$$

Where $E_{cluster}$ is the transverse energy sum in a block of 3×2 Super Cells in the second layer of the calorimeter centred on the local maximum. $E_{environment}$ is the energy of a block of 7×3 Super Cells centred on the same maxima. From fig. 4b, S_0 would be the local maxima, the dashed rectangle shows the 3×2 block of Super Cells used for $E_{cluster}$ and the dotted rectangle shows the 7×3 block of Super Cells used for $E_{environment}$.

R_{Had} defines the ratio of energy deposited within the hadronic calorimeter to the electromagnetic calorimeter and is calculated using:

$$R_{Had} = \frac{E_{Hadronic}}{E_{Hadronic} + E_{EM}} \quad (3)$$

E_{EM} is the summed energy of the 4 layers of the EM calorimeter. This follows the same definition as used in the seed finding algorithm, summing a 1×2 Super Cell block in the pre-sampler and third layer, and a 3×2 block in the first and second layer. $E_{Hadronic}$ is the energy deposited in a region $\Delta\eta \times \Delta\phi = 0.3 \times 0.3$ in the Hadronic calorimeter behind the EM energy cluster.

The W_{STot} parameter measures the cluster width within the first layer of the calorimeter. The value is calculated according to:

$$W_{STot} = \sqrt{\frac{\sum_i E_i (i - i_{max})^2}{\sum_i E_i}} \quad (4)$$

Which is the ratio of the grid distance weighted sum of the energy deposit to the total energy deposit of the cluster. The sum runs over 5 adjacent Super Cells in η centred on the maximum energy Super Cell in the first layer of the calorimeter.

The FPGAs record the cluster's position(η and ϕ), energy and isolation. Three levels of isolation working points are implemented: Loose(L), Medium(M), and Tight(T) and represent cuts made on the shower shape algorithms. Each working point contains identified objects that are a subset of the previous, looser working point, with the identification criteria becoming stricter with each step. The information for all generated RoIs are sorted across the whole eFex system and are then sent to further L1 modules for data processing. RoIs that pass the L1 trigger criteria are sent to the HLT for further processing. The HLT makes a final decision using the full calorimeter and inner detector data. The key feature of photon identification is that, due to them being electrically neutral, they do not leave a track in the inner detector.

1.6.2 New 2025 Isolation Parameter - RHadV2

The L1 eFex group introduced a change to the R_{Had} variable calculation. The new isolation variable changed the sum to include only one Super Cell in the pre-sampler layer and the third layer of the calorimeter has now been included in the E_{Hadronic} calculation. The data for the trigger efficiency measurements has been re-simulated to reflect this change for all of the data taking since October 2024.

1.7 Tag and Probe Method

Measuring trigger efficiencies uses a data driven approach. The Tag and Probe[5] method uses a well understood resonance; in the case of photons, the $Z \Rightarrow e(e + \gamma)$ resonance, Fig. 5 shows the Feynmann diagrams of the possible final state. The Z boson decay is a well studied decay with a low background interference making it a useful decay to study the detector performance.

The method uses the resonance to produce an electron, positron and photon which can be used to test trigger configurations. The electron or positron are used as the tag, they are required to have a high likelihood of being correctly identified and must have triggered the event. The photon is the probe and can have looser identification criteria.

The discriminating variable, between signal and background, is the invariant mass of the three particles in the data. An electron, positron and photon are chosen from the data if their combined invariant mass is close to the Z boson mass and falls in the range $\approx \pm 15\text{GeV}$ around the Z mass.

The idea is that if a resonance containing two clean leptons and a photon is found, and the trigger fired on the leptons then the sample of photons produced is expected to be pure and unbiased. This allows unbiased and accurate tests of the trigger conditions on these photons.



Figure 5: Feynman diagrams for the $Z \Rightarrow e(e + \gamma)$ final state radiation resonance used in the tag and probe method for photons. The photon can radiate from either the electron or positron.

1.8 Event Selection

Following the selection in Ref. [6], selection requires two oppositely charged leptons with $p_t > 10\text{GeV}$. The leptons must pass a Medium identification criteria, be inside the fiducial region of the detector $|\eta| < 2.47$ and must not be within the calorimeter transition region, defined as $1.37 < |\eta| < 1.52$. The leptons must also have passed the electron trigger chain in the HLT; removing events where the photon fakes an electron in the trigger.

The photons must pass a tight identification working point and must have $p_t > 7\text{GeV}$. The photons must also lie in the fiducial region and not in the calorimeter transition region. Further, as particle reconstruction is run independently for all particle types photons overlapping with electrons are removed, requiring $\Delta R > 0.2$ between the photon and either lepton. $\Delta R > 0.2$ chooses isolated objects in the

calorimeter, different from trigger isolation. ΔR is the distance between detected objects:

$$\Delta R = \sqrt{(\Delta\eta)^2 + (\Delta\phi)^2} \quad (5)$$

Where $\Delta\eta$ is the difference in η and $\Delta\phi$ is the difference in ϕ between the lepton and photon.

The event selection is for FSR photons. To reject ISR photons, the two lepton invariant mass must satisfy $m_{\ell\ell} < 82\text{GeV}$. Fig. 6a shows the distribution of events of the two lepton invariant mass against the three particle invariant mass, with the shaded region used for selection. The horizontal band centred at $m_{\ell\ell} \approx 90\text{GeV}$ highlights $Z \rightarrow \ell\ell$ decays with ISR photons. The vertical band centred at $m_{\ell\ell\gamma} \approx 90\text{GeV}$ highlights decays with FSR photons.

An event is then chosen that lies within $\pm 15\text{GeV}$ of the Z mass. If, in the unlikely event, there is more than 1 possible combination of photons, electrons, or positrons after this selection, the combination with an invariant mass closest to the Z mass is chosen. In total, 51356 FSR photons were extracted from 12.2fb^{-1} of ATLAS data.

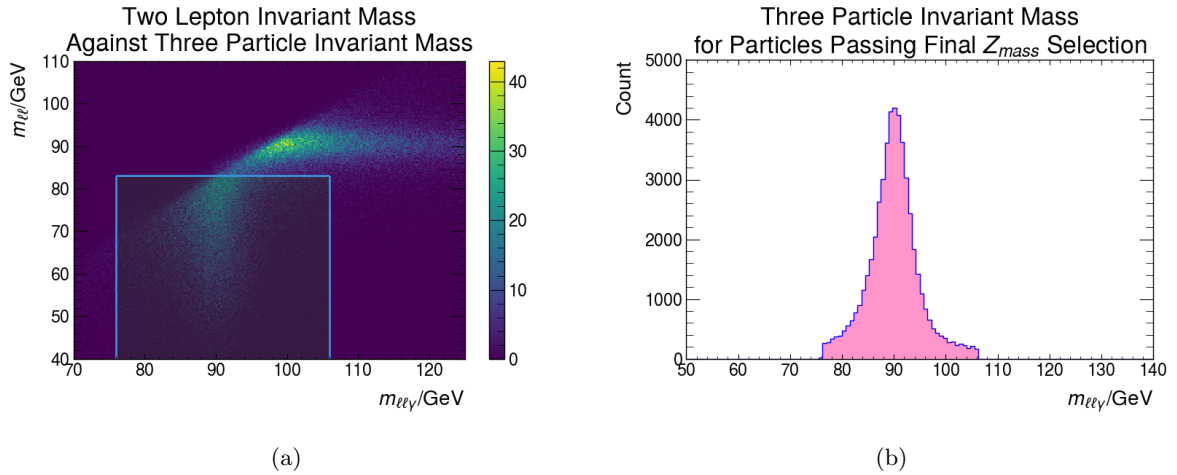


Figure 6: (a) Distribution of two lepton invariant mass($m_{\ell\ell}$) against three particle invariant mass($m_{\ell\ell\gamma}$). The increased density vertical band contains final state radiation events and the increased density horizontal band contains $Z \rightarrow \ell\ell$ events with an initial state radiation photon. The outlined and shaded region shows the region of the space that the signal photons are extracted from. (b) Final three particle invariant mass $m_{\ell\ell\gamma}$ plot after a complete event selection.

1.8.1 Photon Trigger Matching

Photons are first matched to any RoI generated by the L1 eFex system. A match is accepted if the photon is within $\Delta R < 0.2$ of the RoI. Once a match is found the trigger conditions can be emulated by testing the isolation and the energy of the calorimeter deposit. The isolation of the RoI is measured against three working points: Loose, Medium or Tight. The energy deposit of the RoI is tested against the energy threshold for a specific trigger.

1.8.2 Monte Carlo Dataset Event Selection

Monte Carlo datasets can generate events for specific decay processes, simulate detector conditions and run particle reconstruction. Reconstructed particles can then be tested against 'truth' particles which were created during event generation. Further, simulation allows the classification of particles based on their type and origin[25]. For trigger efficiency analysis, the Monte Carlo datasets can be used to estimate the interference of fake or non-FSR photons in the event selection described in Section 1.8.

Reconstruction follows Section 1.8. In total, 4946 FSR photons were extracted from the Monte Carlo sample. The selected electron, positron and photon are then matched to truth particles, $\Delta R < 0.2$. Then, lepton classification is checked for prompt leptons originating from a Z boson decay. The matched truth photon must be classified as a FSR photon. Two Monte Carlo datasets[26, 27, 28, 29] are used for the analysis, a $Z \rightarrow ee$ [30] and a dijet sample[31].

2 ATLAS Photon Trigger Performance Measurements

2.1 Trigger Efficiencies

With reduced available information and a requirement for fast identification, L1 triggers show a lower particle identification performance than offline reconstruction algorithms. The trigger response has a turn on curve, selection starts around a threshold energy, increasing as cluster energy exceeds the threshold. Efficiency approaches but does not always reach 100% efficiency. The optimal curve would be a vertical line to 100% efficiency at the specified cluster energy threshold. This is not possible due to the difference in energy resolution between L1 clusters and offline reconstructed photons. The introduction of Super Cells significantly improved the energy resolution at L1 allowing sharper turn on curves and lowering the offline photon p_t analysis threshold for the same trigger rate[11]. Triggers bias data taking towards selection of useful EM objects however an efficiency curve that asymptotes well below 100% can indicate a bias towards certain physical processes, possibly causing the detector to miss key physics. For physics analysis, offline photon candidates are chosen when the L1 trigger reaches $\approx 90\%$ efficiency. Events signalled before this level are wasted rate and as such a key aspect with trigger curves is to have a steep turn on that rapidly reaches 90% efficiency before plateauing.

2.1.1 Efficiency Statistics

Photon trigger selection efficiency can be measured by considering a set of Bernoulli's random variables[32]. The probability of k successes given n trials with a selection efficiency ϵ is then given by the binomial formula.

$$P(k|\epsilon, n) = \binom{n}{k} \epsilon^k (1 - \epsilon)^{n-k} \quad (6)$$

Bernoulli's weak law of large numbers states that in the limit of an infinite number of trials the selection efficiency tends towards the ratio of successes of a Bernoulli trial to the total number of trials[33],

$$\epsilon = \frac{k}{n} \quad (7)$$

If the selection efficiency needs to be measured with respect to some parameter, x . The standard method is to generate histograms of events passing the selection, k_i , and the total number of trials, n_i . The bin by bin selection efficiency ϵ_i is then estimated from the ratio of k_i successes and n_i trials in each bin.

$$\epsilon(x_i) \approx \frac{k_i}{n_i} \quad (8)$$

The confidence intervals are chosen to be calculated using Clopper-Pearson confidence intervals. They are an exact method based on the inversion of the cumulative binomial distribution. Clopper-Pearson confidence intervals guarantee coverage but are susceptible to over covering the uncertainty.

2.1.2 New Efficiency Curve Fitting Method

If the selection efficiency is hypothesised to be a function of some parameter, θ . A model can be fit to data via maximum likelihood estimation (MLE). The selection efficiency function, $\epsilon(x, \vec{\alpha})$, that best fits the data is the function parameters that minimise the total binomial negative log likelihood across all data points.

$$\min_i \sum -\log(L(\epsilon(x_i, \vec{\alpha})|k_i, n_i)) \equiv \min_i \sum (-k_i \log \epsilon(x_i, \vec{\alpha}) - (n_i - k_i) \log (1 - \epsilon(x_i, \vec{\alpha}))) \quad (9)$$

Here, $L(\epsilon(x_i, \vec{\alpha})|k_i, n_i)$ is the likelihood of the efficiency at a point x_i given k_i successes and n_i trials. $\epsilon(x_i, \vec{\alpha})$ denotes the efficiency as a function of the position x_i and the parameters of the function $\vec{\alpha}$. $-\log \binom{n}{k}$ has been omitted as it does not depend on ϵ .

Using MLE, the photon p_t at key points on the efficiency curve can be measured. There is no consensus on the exact mathematical function that describes a full efficiency curve. The isolated trigger efficiency

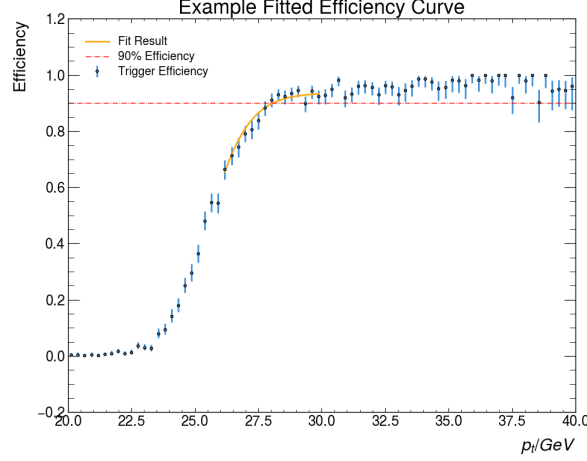


Figure 7: Example fit of an efficiency curve using the new fitting method for a trigger energy threshold of 25GeV and Medium isolation, targeting the photon p_t at 90% trigger efficiency. The 90% efficiency level is highlighted.

curves appear to follow a similar shape to an integrated skew normal distribution or an exponentially modified Gaussian distribution. Trigger isolation further convolutes the exact mathematical form of an efficiency curve and the form can vary with energy. In order to estimate offline photon p_t at key points on the trigger efficiency curve, 10%($E_{10\%}$), 50%($E_{50\%}$) and 90%($E_{90\%}$) efficiency. The efficiency curves were fit in a reduced region around the efficiency level of interest. The eFex subgroup currently fit using a Fermi function, which has a similar shape to a Gaussian CDF and as such a Fermi function was used on the reduced range. The fitting algorithm works as follows:

1. Iterate through the efficiency curve
 - Find the first bin that within error surpasses the efficiency threshold and create a lower bound 2GeV below this bin
 - Find the first bin that has an average bin efficiency above the efficiency threshold and create an upper bound 2GeV above this bin
 - Find the first bin that within error surpasses the 0.5 efficiency threshold denoted β_0
2. Initialise a fermi function with $\alpha = 1$, $\beta = \beta_0$, $\gamma = 1$

$$E = \frac{\alpha}{(1 + e^{\frac{(\beta - x)}{\gamma}})} \quad (10)$$

3. Fit the fermi function to the efficiency points using Eq. 9 and MLE within the upper and lower bound
4. Determine the x value intercepting the efficiency threshold, E

$$x = \beta - \gamma \ln\left(\frac{\alpha}{E} - 1\right) \quad (11)$$

Error estimation uses Monte Carlo. Sample parameters are drawn from the multivariate normal distribution using the covariance matrix of fit results. The intercept is calculated from Eq. 11 and the standard deviation of the distribution of intercept values quantifies the error. Fig.7 demonstrates the fit on a 25 GeV threshold, Medium isolation trigger.

2.1.3 Trigger Performance Measurements

L1 trigger efficiency is measured by binning photons that have passed a trigger's criteria and photons that have passed the event selection criteria in transverse momenta. Curves are generated for both an isolated and unisolated trigger, with an unisolated trigger representing the best possible selection efficiency available at L1. Isolation performance impact is measured by measuring the offline photon p_t

when the trigger efficiency surpasses 90% (denoted offline photon p_t at 90% trigger efficiency or $E_{90\%}$). If the p_t is lower than the photon p_t used for offline analysis, the trigger is not performing sufficiently.

For η efficiency measurements, photons are divided into η bins and transverse momenta efficiency curves are generated for each bin. To assess performance variation, the photon transverse momenta at 90% trigger efficiency is used as a comparable variable between η bins. The trigger performance across η bins should be equal within tolerance. An increased photon p_t at 90% trigger efficiency in one η bin compared to other η bins, or a trend of increased energies would show that the trigger performance is being negatively affected within specific η bins. The photons are split into η regions based on an equal frequency method.

1. Photons are filtered to have offline transverse momenta at least 7GeV below and no more than 30GeV above the trigger energy threshold
2. The photons are sorted from low to high according to their corresponding η value
3. The target population per bin is determined by dividing the total number of photons by the number of η bins used to evaluate performance. $n = \frac{n_{\text{photons}}}{n_{\text{bins}}}$
4. The η ordered photons are split by setting the bin boundaries to the η values at indices spaced every n elements apart starting from the first index.

For pileup performance measurements, photons are split into pileup regions based on actual measured pileup using the a similar equal frequency binning procedure as for the η measurements. For each pileup region, the photons are tested against trigger criteria, efficiency curves are constructed for the specific trigger, the photon p_t at 90% trigger efficiency is then used as a measure of performance in specific pileup regions. An increased photon p_t where the trigger reaches 90% efficiency indicates a worse performing trigger.

The performance of trigger isolation levels with respect to the cluster energy threshold of a trigger has been measured. The collection of photons and their corresponding L1 clusters are tested against trigger thresholds from 10GeV to 30GeV, and for each isolation Loose, Medium and Tight. Trigger curves with respect to transverse momenta are generated for each combination of cluster energy threshold and isolation requirement. The p_t at 90% trigger efficiency is then measured for each generated efficiency curve.

2.2 Results

2.2.1 Sample Purity

Fig. 8 shows the p_t distribution for photons passing event selection and truth photons derived from a Monte Carlo sample containing 1.99 million $Z \rightarrow ee$ events. The Monte Carlo sample agrees with the data for low $p_t < 15\text{GeV}$, higher p_t shows the MC overestimating the data. Fig. 8b shows efficiency of selecting true photons using the event selection criteria described in section. 1.8 against offline photon p_t . The efficiency curve reaches 95% efficiency at $(15.4 \pm 1.1)\text{GeV}$. Given the lowest trigger has a cluster energy threshold of 15GeV, the sample purity at 90% trigger efficiency should be above 95% for this trigger. For higher energy triggers, the purity will increase.

The sample purity measurement looks solely at the coincident photon rate, the number of events that contain a photon that is not released from either of the leptons in the event. The measurement fails to account for fake rate of leptons and photons caused by jets generated in the detector. A sample of 1 million Monte Carlo generated soft QCD jets was tested against the event selection criteria, however no candidates passed the event selection criteria. This is most likely due to the fact that the jet reconstruction and identification algorithms within ATLAS are very good and therefore rejection is very high. However, soft QCD jets in ATLAS have a very high cross section, Monte Carlo samples[31] use 78.6mb, which means that whilst the probability of selecting these events are low, there are overwhelmingly many events produced which can influence the data. There are also more processes that would be required for a full treatment of estimating the true total sample purity[34].

2.2.2 Efficiency Curves

The main level 1 trigger efficiencies have been measured and are displayed in Fig. 9. All the triggers start at zero efficiency. The turn on starts before the trigger energy threshold due to the difference in energy resolution between level 1 and offline reconstructed photons. The triggers all reach above 95% efficiency

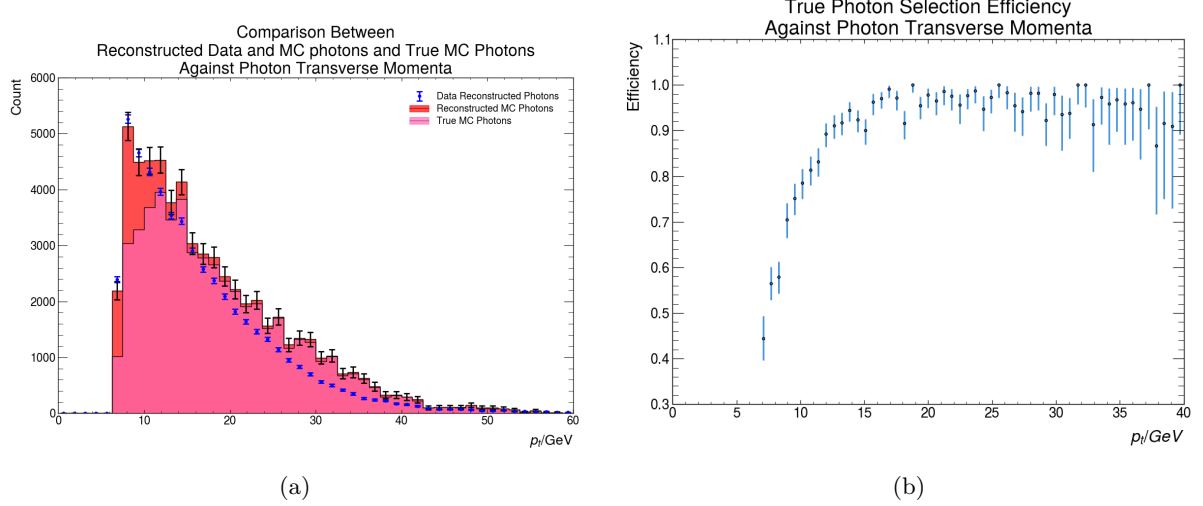


Figure 8: (a) Plot of the results from a 1.99 million event Monte Carlo dataset showing the offline photon p_t distribution of photons passing the event selection criteria and those which are matched to truth photons tagged as FSR photons by the MC event generator. The Monte Carlo photon distribution is compared to the distribution of photons derived directly from ATLAS data. (b) The variation, with respect to photon p_t , in the efficiency of selecting true, FSR and non coincident photons. The efficiency value highlights the sample purity.

and asymptote towards 100% efficiency. The eEM26M trigger Fig.9a will be above 99% efficient at the HLT cut off of 140 GeV. The eEM24L trigger is 90% efficient at 25 GeV and will be above 98% efficient at 35 GeV. The eEM18M trigger Fig.9c shows a slower turn on compared to the eEM26M and eEM24L. The eEM18M trigger is above 90% efficiency for physics analyses starting at 20 GeV and reaches 95% efficiency for analysis starting at 22 GeV. Table 1 summarises the main efficiency points on the trigger curve.

Trigger Name	$E_{10\%}/\text{GeV}$	$E_{50\%}/\text{GeV}$	$E_{90\%}/\text{GeV}$
eEM18M	14.50 ± 0.03	15.94 ± 0.03	19.1 ± 0.6
eEM24L	20.98 ± 0.04	22.69 ± 0.03	25.1 ± 0.1
eEM26M	23.80 ± 0.05	25.56 ± 0.04	27.8 ± 0.1

Table 1: Table of the p_t for the key selection efficiency points on the trigger turn on curves. The points measured are offline photon p_t at 10% ($E_{10\%}$), 50% ($E_{50\%}$) and 90% ($E_{90\%}$) trigger efficiency.

2.2.3 Pseudo rapidity Trigger Performance

Fig.10 shows the performance variation of the main photon triggers with η . The event selection removes photons detected in the transition region $1.37 < |\eta| < 1.52$. Measurements across that region use data from the surrounding regions. The eEM26M trigger is uniform in η to 2σ errors. There appears to be a slight rise in the photon p_t at 90% trigger efficiency ($E_{90\%}$) around the transition region. The eEM24L trigger is uniform across η to 2σ errors. There is a more prominent $E_{90\%}$ increase around the transition region however within errors the performance is the same. The eEM18M trigger is uniform to 2σ uncertainty. There is a more significant decrease in trigger performance around the transition region than for the other triggers. The area surrounding the transition region lies 2σ above the average with an approx. 1GeV increase in $E_{90\%}$ compared to the average performance. The average performance, 1σ performance variation, Maximum $E_{90\%}$ and minimum $E_{90\%}$ in η is shown in Table 2.

2.2.4 Pileup Trigger Performance

The pileup dependent measurements of the eEM18M, eEM24L and eEM26M show that within 1σ uncertainty the photon p_t at 90% trigger efficiency ($E_{90\%}$) coincides with the confidence interval of the error weighted average of $E_{90\%}$ across all pileup regions. The average photon $E_{90\%}$ measurements for the

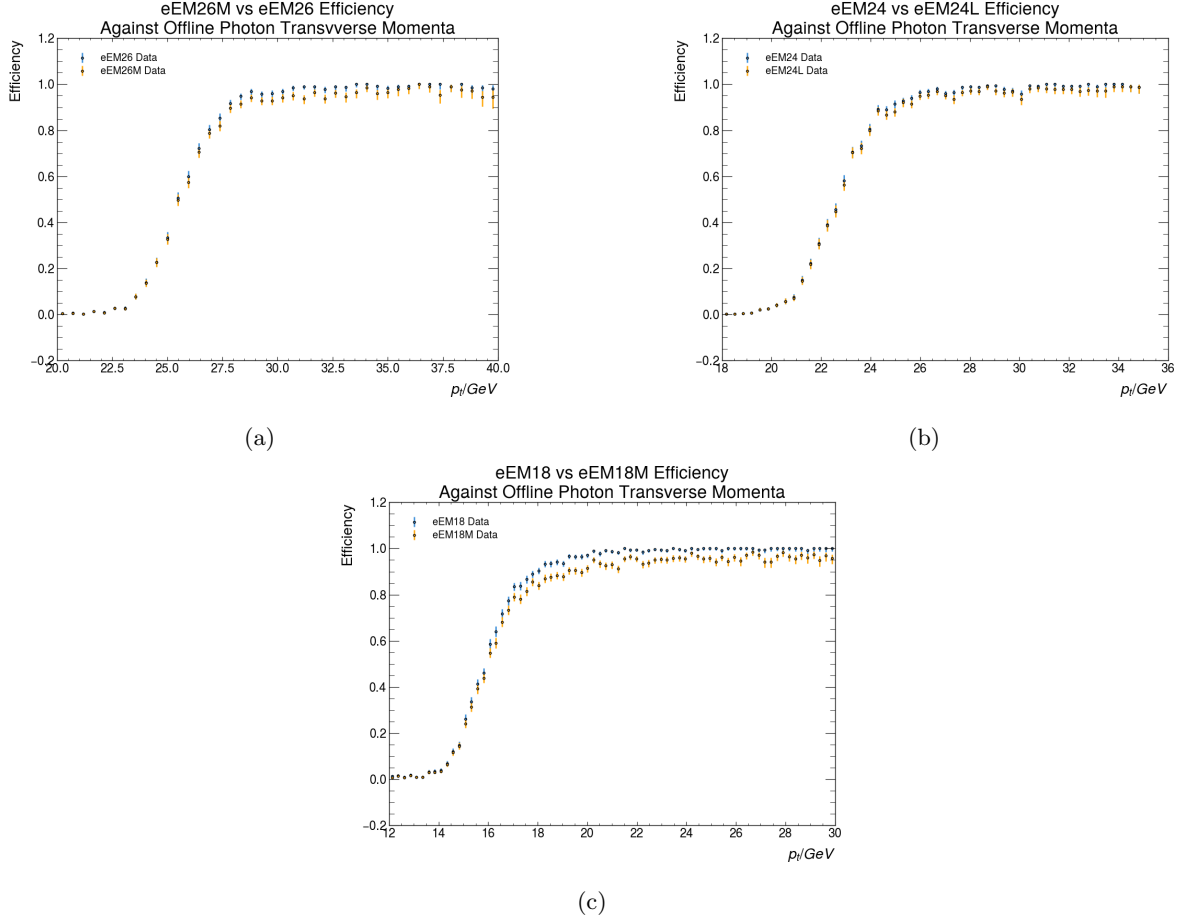


Figure 9: Plots of efficiency against offline photon transverse momenta for the eEM26M (a), eEM24L (b) and eEM18M (c) triggers. The blue data shows the same trigger but without isolation, the blue shows the trigger efficiency being measured. The uncertainties are Clopper-Pearson 68.3%(1 σ) confidence intervals.

triggers are displayed in table 3. There could be considered a decrease in the trigger performance with pileup. The maximum variation being ≤ 2.3 GeV for all triggers from 7 to 80 interactions per bunch crossing shows that the effect of pileup is very weak at the current pile up within ATLAS.

2.2.5 Trigger Isolation Threshold Performance

Fig. 12a shows the variation of the trigger performance with respect to a choice of trigger cluster energy threshold, $E_{\text{Threshold}}$. The green line shows a linear fit to the unisolated trigger performance measurement. The unisolated trigger $E_{90\%}$ is approximately directly proportional to the cluster energy threshold, with an offset.

$$E_{90\%} \approx (0.99 \pm 0.002)E_{\text{Threshold}} + (2.90 \pm 0.03) \quad (12)$$

Therefore non-linear effects on $E_{90\%}$ can be solely attributed to the application of isolation. The

Trigger Name	Average $E_{90\%}$ /GeV	1σ Maximum $E_{90\%}$ Variation/GeV	Maximum $E_{90\%}$ /GeV	Minimum $E_{90\%}$ /GeV
eEM18M	18.6 ± 0.2	4.2	21.4	17.2
eEM24L	24.7 ± 0.1	3.0	26.9	23.9
eEM26M	27.6 ± 0.1	3.5	30.6	27.0

Table 2: Table of the main performance metrics considered for comparing the variance of the trigger efficiency in η . The performance is measured by the offline photon p_t at 90% trigger efficiency ($E_{90\%}$)

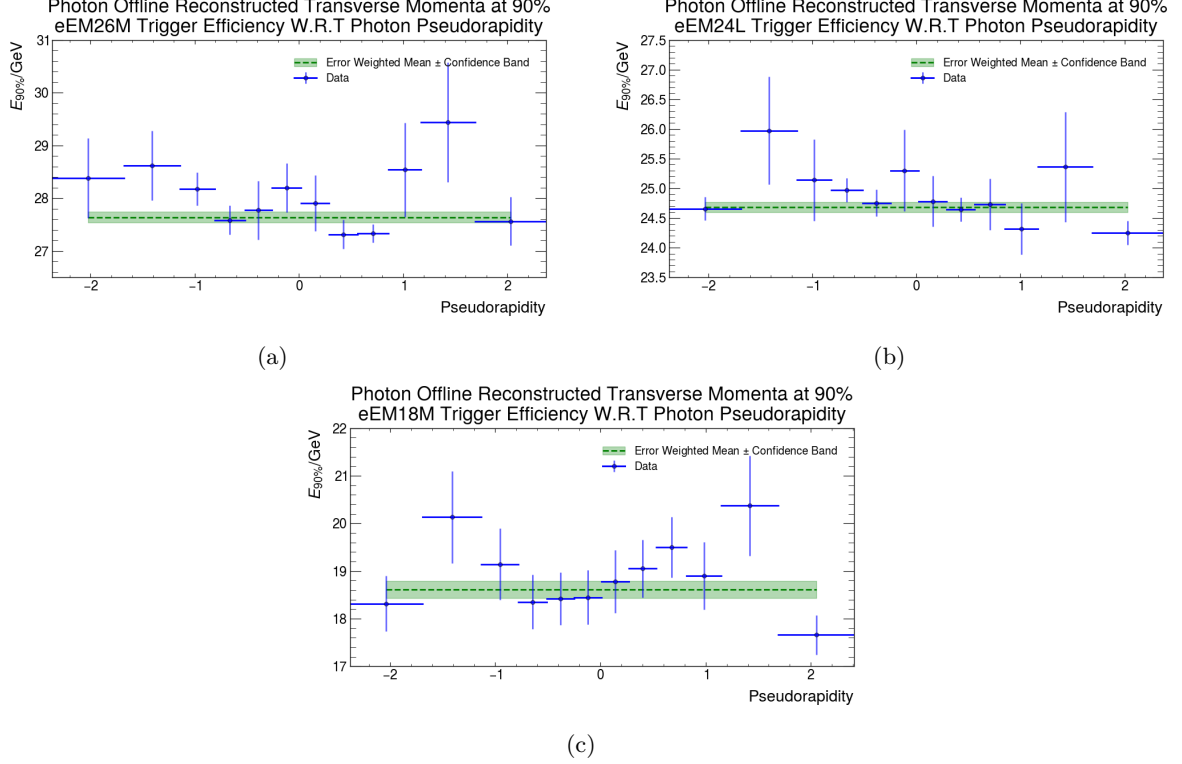


Figure 10: Plots of offline photon transverse momenta at 90% photon trigger selection efficiency against η for the eEM26M (a), eEM24L (b) and eEM18M (c) triggers. Uncertainties are shown as 1σ uncertainties from multivariate Monte Carlo on the maximum likelihood parameter errors. The horizontal blue lines show the width of the bins being tested using equal frequency binning. The green dashed line shows the error weighted average and the 68.3%(1σ) confidence interval.

data points in Fig. 12a for each level of isolation are minimally offset to make it easier to compare. Fig. 12b shows the residual of the isolated $E_{90\%}$ from the unisolated $E_{90\%}$ linear fit, green dashed line. The residuals have been fitted with their error weighted average for $E_{\text{Threshold}} \geq 18\text{GeV}$. The non linear divergence from isolation (to 1σ) occurs below 18GeV for Tight and Medium isolation and occurs below 17GeV for the loose isolation.

Below 17GeV, Tight isolation performance is reduced such that for $13\text{GeV} \leq E_{\text{Threshold}} \leq 16\text{GeV}$ $E_{90\%}$ is equal (to 1σ), increasing rate with no performance gain. Tight isolation trigger performance degrades from $E_{\text{Threshold}} = 18\text{GeV}$ down to 13GeV. This means that Tight isolation is not feasible to be used for triggers below 18GeV. Performance cannot be accurately evaluated below $E_{\text{Threshold}} = 13\text{GeV}$ as the sample purity decreases below approx. 80%.

Medium isolation $E_{90\%}$ diverges for $E_{\text{Threshold}} \leq 18\text{GeV}$ however below 15GeV the trigger performance degrades such that $E_{90\%}$ is equal (to 1σ) for all $13\text{GeV} \leq E_{\text{Threshold}} < 15\text{GeV}$. The divergence does mean that Medium isolation causes a reduced trigger turn on speed at low p_t . Loose isolation diverges $E_{90\%}$ at 17GeV. The divergence is less than for Medium and Tight isolation. Loose isolation trigger performance does not degrade sufficiently such that $E_{90\%}$ is equal (to 1σ) for any range of $E_{\text{Threshold}}$.

Trigger Name	Average $E_{90\%}/\text{GeV}$	1σ Maximum $E_{90\%}$ Variation/ GeV	Maximum $E_{90\%}/\text{GeV}$	Minimum $E_{90\%}/\text{GeV}$
eEM18M	18.8 ± 0.2	2.0	19.9	17.9
eEM24L	24.9 ± 0.1	0.9	25.4	24.5
eEM26M	28.1 ± 0.1	1.8	29.4	27.7

Table 3: Table of the main performance metrics considered for comparing the variance of the trigger efficiency in pileup(μ). The performance is measured by the offline photon p_t at 90% trigger efficiency ($E_{90\%}$)

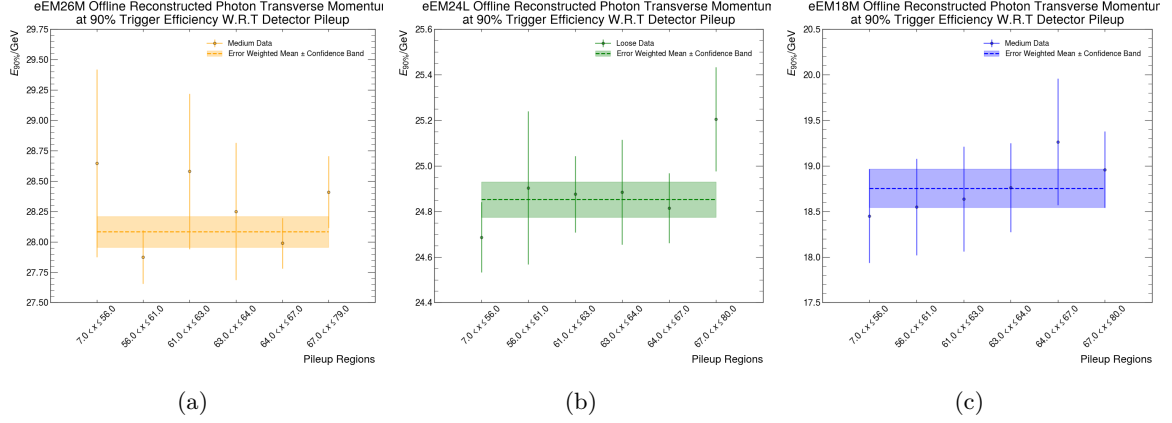


Figure 11: Plots of offline photon transverse momenta at 90% trigger efficiency ($E_{90\%}$) against pileup for the eEM26M (a), eEM24L (b) and eEM18M (c) triggers. Bins are sized using equal frequency binning. Uncertainties are shown as 1σ uncertainties from multivariate Monte Carlo on the maximum likelihood fit parameter errors. The horizontal dashed lines shows the error weighted average and the 68.3%(1 σ) confidence interval.

3 Trigger Isolation Tuning Algorithm

Section 2.2 highlighted that the performance of low $E_{\text{Threshold}}$ triggers, especially the eEM18M trigger, is reduced by the application of Medium isolation criteria. Isolation tuning previously focussed on tuning the eEM26M trigger using electrons from $Z \rightarrow ee$ decays. This could cause the decreased performance for the eEM18M trigger. The project aimed to generate a tuning algorithm that can be applied to photons at lower p_t , when the current isolation parameters show reduced performance. The algorithm and it's results are outlined in this section including a comparison to the current Medium isolation that is used at L1.

3.1 Trigger Isolation Tuning

Isolation working points are tuned on data. The FPGAs output an 8-bit integer between 0 and 255 for each isolation variable from Section 1.6.1. The firmware is currently limited to independent parameter thresholds and a single threshold value for each parameter as they are easier to implement on FPGAs. Background rejection is achieved by choosing cuts on the variables that have a signal selection efficiency lower than 100%. By accepting a lower signal selection efficiency, usually above 90%, there is freedom to choose cuts that minimise the background selection efficiency.

The tuning algorithm considers 3D histograms of the photon and background distributions binned by their isolation coefficients. If each bin is divided by the total number of events, the value can be taken as an effective efficiency per bin. If a volume of the histogram is summed over, the resulting value represents the effective efficiency of that volume. The optimisation works by searching for a volume within the space that satisfies constraints on the signal and background efficiencies. More formally, The signal and background selection efficiency can be calculated by binning events with respect to their 8-bit isolation coefficient and then calculating the bin by bin fraction of events,

$$f_{ijk} = \frac{a_{ijk}}{\sum_{ijk} a_{ijk}} \quad (13)$$

f_{ijk} is the fraction of events in a bin, a_{ijk} represents the number of signal or background events in a bin. The total effective efficiency of a chosen set of thresholds is the sum of the cuboid like region within the histogram contained by the thresholds. If the cuts are represented by a index tuple $\vec{x} = (x_0, x_1, x_2)$ and maxima of the indexes are (255, 255, 255) then the volume efficiency $E(\vec{x})$ for the case of selection above or equal to the isolation cuts is

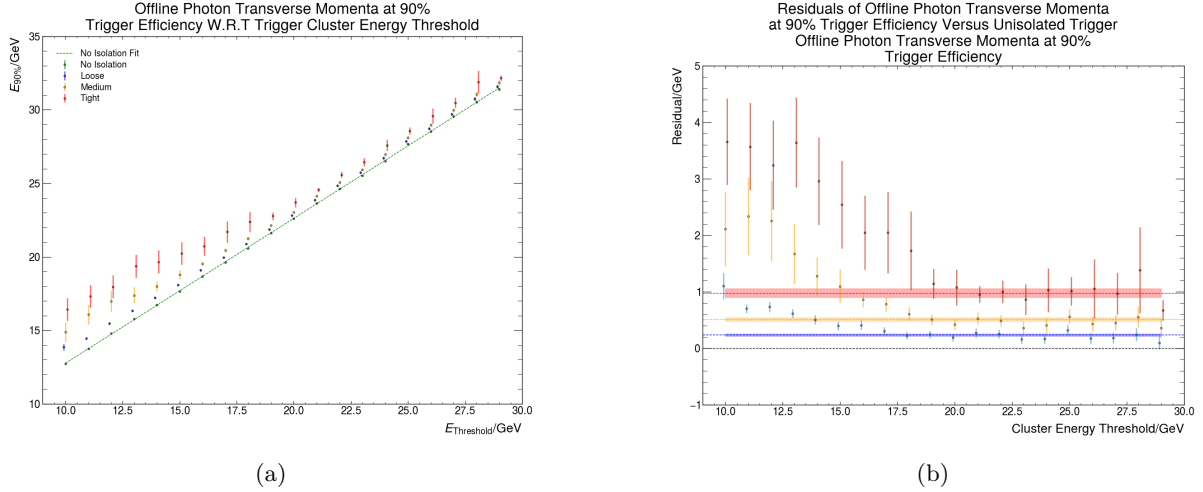


Figure 12: Plot showing the dependence of the offline photon p_t at 90% trigger efficiency ($E_{90\%}$) with trigger energy threshold ($E_{\text{Threshold}}$) and each level of isolation: unisolated. Each level of isolation is slightly offset at every point to aid comparison on overlapping points. (a) The direct trend in $E_{90\%}$ with trigger threshold $E_{\text{Threshold}}$. Uncertainties are shown as 1σ uncertainties from multivariate Monte Carlo on the maximum likelihood parameter errors. The green dashed line shows a linear fit to the unisolated trigger data. (b) Shows the residual of each of the isolation data points to the green dashed line in (a), uncertainties assume negligible errors on the unisolated fit. Horizontal dashed lines show error weighted average with 68.3%(1σ) confidence intervals colour coded to the data points.

$$E(\vec{x}) = \sum_{i=x_0}^{255} \sum_{j=x_1}^{255} \sum_{k=x_2}^{255} f_{ijk} \quad (14)$$

In the case of event selection below or equal to the isolation cuts the efficiency can be calculated as:

$$E(\vec{x}) = \sum_{i=0}^{x_0} \sum_{j=0}^{x_1} \sum_{k=0}^{x_2} f_{ijk} \quad (15)$$

Eq. 14 and Eq. 15, calculates the effective volume efficiency of every possible combination of thresholds. Optimal cuts can then be chosen directly from this data structure as the index of the grid with a effective volume efficiency that satisfies some criteria. Tuning can then be written as a set of constraints on the cuts. As an example one such choice would be:

$$\begin{aligned} &\underset{\vec{x}}{\text{minimize}} && E_{\text{background}}(\vec{x}) \\ &\text{subject to} && E_{\text{signal}}(\vec{x}) \geq 95\% \end{aligned} \quad (16)$$

Direct calculation of all possible combinations of isolation cuts using Eq. 14 or 15 would be incredibly slow, with $O(N^6)$ complexity. The calculation of these quantities is improved to $O(N^3)$ complexity using summed volume tables, described below.

3.2 Summed Volume Tables

Summed volume tables are the 3D generalisation of summed area tables[35, 36]. They are more generally known as the integral image[37, 38]. In image processing, the 2D integral image is defined such that every pixel is replaced with the sum of the pixels above and to the left of that pixel. If the hyper-voxel, the N-dimensional generalisation of a pixel, position is defined by a set of indices $\vec{x} = (x_0, x_1, \dots, x_n)$, $\vec{x} \in \mathbb{N}^n$, the N-dimensional integral image, $I(x_0, x_1, \dots, x_n)$, is defined as

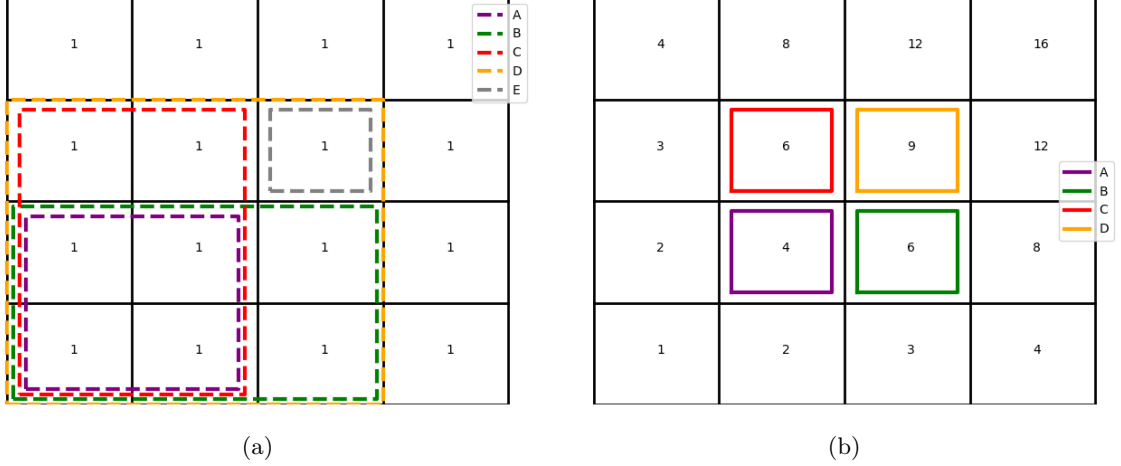


Figure 13: Diagrams showing the process of constructing a summed area table. In (a) The orange region D is calculated by the sum $D = E + B + C - A$ as A is contained in both regions B and C. In (b) the summed area table is shown. The corresponding regions to the grid in (a) is colour coded. Region D is now the upper right grid entry. Region B is one step backwards in the y direction and region C is one step backwards in the x direction in the summed area table. Region A is one step back in both x and y . This aligns with Eq. 18 with $i(x_0, x_1)$ corresponding to region E in (a), $I(x_0 - 1, x_1) + I(x_0, x_1 - 1) - I(x_0 - 1, x_1 - 1)$ correspond to regions B, C and A respectively in both (a) and (b), but taking from (b) the region sum is already contained by the table.

$$I(x_0, x_1, \dots, x_n) = \sum_{j_0=0}^{x_0} \sum_{j_1=0}^{x_1} \dots \sum_{j_n=0}^{x_n} i(j_0, j_1, \dots, j_n) \quad (17)$$

Where $i(j_0, j_1, \dots, j_n)$ is the hyper-voxel value at position j_0, j_1, \dots, j_n . In 2D this can be efficiently calculated recursively by rewriting the summation[37]:

$$I(x_0, x_1) = i(x_0, x_1) + I(x_0 - 1, x_1) + I(x_0, x_1 - 1) - I(x_0 - 1, x_1 - 1) \quad (18)$$

This can be understood by considering overlapping regions. The sums $I(x_0 - 1, x_1)$ and $I(x_0, x_1 - 1)$ both include the sum $I(x_0 - 1, x_1 - 1)$. Hence, we subtract $I(x_0 - 1, x_1 - 1)$ once to account for double counting. Fig. 13 shows diagrams of this process in 2D, each region in Fig. 13a represents an area summed over. Eq. 18 is then the equivalent to the sum of the regions $D = E + B + C - A$ from Fig. 13a. Regions A, B and C can be extracted from previously calculated values in the summed volume table, as shown in Fig. 13b.

The recurrence can be extended to the 3D case[39],

$$\begin{aligned} I(x_0, x_1, x_2) = & i(x_0, x_1, x_2) + I(x_0 - 1, x_1, x_2) + I(x_0, x_1 - 1, x_2) + I(x_0, x_1, x_2 - 1) \\ & - I(x_0 - 1, x_1 - 1, x_2) - I(x_0 - 1, x_1, x_2 - 1) - I(x_0, x_1 - 1, x_2 - 1) \\ & + I(x_0 - 1, x_1 - 1, x_2 - 1) \end{aligned} \quad (19)$$

The extension to 3D can be understood in the same way as the 2D case however it is the overlap of three sums. The sums $I(x_0 - 1, x_1, x_2)$, $I(x_0, x_1 - 1, x_2)$ and $I(x_0, x_1, x_2 - 1)$ overlap the same way as in the 2D case and therefore you must subtract double counted regions e.g $I(x_0 - 1, x_1 - 1, x_2)$. Both the added and subtracted regions contain the sum $I(x_0 - 1, x_1 - 1, x_2 - 1)$, cancelling each other, meaning it needs to be re-added at the end.

Summed volume tables allow rapid calculation of the selection efficiency for all possible parameter cuts. Optimal solutions can then be read directly from the index position of the SVT element that satisfies the effective efficiency signal and background criteria. The summed volume table also has another useful property, the sum of sub regions can be calculated in $O(1)$ complexity by using 8 points from summed volume table[36].

3.3 Implementing New Level 1 Trigger Tuning Algorithm

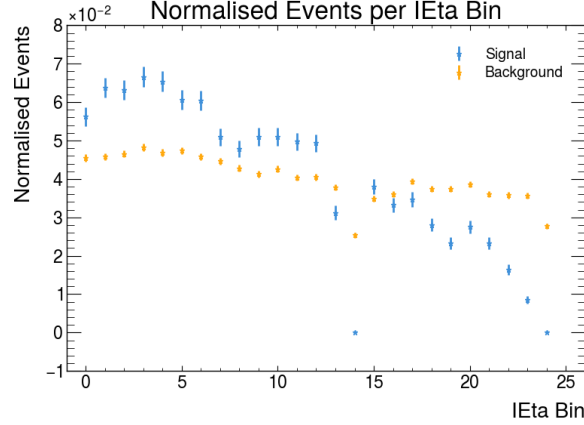


Figure 14: Plot showing the normalised distribution of events in each IEta bin for signal events (blue) and background (zero bias) events (orange). Uncertainties use 1σ Poisson statistics. bins 14 and 24 are excluded from event selection, zero signal events.

Section 3.1 showed a method to measure the total efficiency of a specific set of parameter cuts, Eq.14 and 15. For trigger isolation, the L1 calorimeter is divided into 50 pseudorapidity regions of width 0.1η , spanning $-2.5 \leq \eta \leq 2.5$, called IEta bins. The regions are considered symmetric about 0, bins with same $|\eta|$ range are combined, reducing the tuning to 25 bins, improving statistics. Signal and background distributions across the 25 IEta bins are shown in Fig. 14. The non uniform distribution in each bin requires correction to total efficiencies using an event weighted average of IEta efficiencies.

$$E_{\text{total}} = \frac{\sum_{i=0}^{24} \omega_i \varepsilon_i}{\sum_{i=0}^{24} \omega_i} \quad (20)$$

Where ω_i is the events in each η bin and ε_i is the efficiency in each η bin.

Optimisation targets a certain p_t range of photons. The efficiency of the isolation should be as high as possible in the turn on stage of the trigger, when the trigger needs to rapidly reach above 90% efficiency. As such, it is best to target photons in a p_t range from the trigger threshold to the point where the trigger surpasses 90% efficiency, statistics need to be considered to get a sufficient sample for tuning.

Isolation thresholds are turned off, any cluster passes the trigger, when a calorimeter cluster energy(E_t) surpasses 60GeV. Therefore, tuning background selection efficiencies on cluster energies $15 < E_t < 60\text{GeV}$ is best. Clusters below 15GeV are rejected by the trigger energy threshold. 55325 background events with $15 < E_t < 60\text{GeV}$ were drawn from 12.2fb^{-1} of ATLAS data using the ZeroBias trigger, a trigger that accepts any detected events randomly. The new algorithm is used to improve the eEM18M trigger, as such the signal selection efficiency is tuned for photons in the range $15\text{GeV} \leq p_t \leq 25\text{GeV}$. 9449 photons in this range were drawn from 12.2fb^{-1} of ATLAS data, using the Section 1.8 event selection. The result of section 2.2.1 showed a 95% sample purity of non coincident photons in this p_t range, showing the tune shouldn't be affected by impurity.

The proposed algorithm needs be tuned to an overall signal and background efficiency target. Firstly, it would be optimal to target the same signal efficiency within each η bin so that the L1 trigger does not penalise signal selection based on the detected cluster position in η . This reduces the number of free parameters as each η bin will have the same target efficiency. For use within the L1 calorimeter, the rate of the new tune should not increase relative to the previous parameter tuning.

3.3.1 Rate Calculations

Rate is calculated using the measured rate of the unisolated eEM18 trigger, with an average peak rate of $295 \pm 2.2\text{kHz}$. The rates of the isolated triggers are then measured as the fraction of events satisfying the selected trigger criteria to the fraction of events satisfying the eEM18 trigger. The rate estimates are made using events from the ZeroBias dataset that satisfy the trigger criteria.

$$R_{\text{trigger}} = R_{\text{eEM18}} \cdot \frac{E_{\text{trigger}}}{E_{\text{eEM18}}} \equiv R_{\text{eEM18}} \cdot \varepsilon_{\text{trigger}} \quad (21)$$

R_{trigger} is the rate of the selected trigger, R_{eEM18} the measured eEM18 rate, E_{trigger} denotes ZeroBias events passing the selected trigger, E_{eEM18} denotes ZeroBias events passing the eEM18 trigger and $\varepsilon_{\text{trigger}}$ the trigger efficiency compared to the eEM18 trigger. As rate is calculated like an efficiency, Clopper-Pearson intervals are used for the uncertainty.

3.4 Monte Carlo Cross Validation

Optimal cuts are made on a sample dataset. Thus, the results will be biased if performance is tested on the data that was used to tune the model. The generalisation of the model to new data can be estimated with the use of Monte Carlo cross validation (MCCV)[40], a method that randomly splits the sample into a test and training dataset repetitively, performing optimisation and testing on each random sample.

The Monte Carlo cross validation method followed the following steps:

1. Select signal and background events from an η bin.
2. Divide the signal events randomly into a training and test dataset using NumPy random.choice, with a ratio between test and training data size of α .
3. Divide the background events into a training and test dataset with the same ratio α
4. Histogram the training and test datasets with respect to each event's isolation coefficients
5. Construct the SVTs for the training and test histograms
6. Extract the index position of the SVT elements satisfying the selection criteria
7. Extract signal and background selection efficiencies from the test dataset SVTs
8. Store the selection efficiencies and the optimal parameters chosen by the model
9. run step 2 to 8 for n samples

MCCV can test the spread of the optimal parameters and the tune performance average and variance across IEta bins. The results should show the stability of the solutions if the distribution of background and signal events is only expected to change due to statistical fluctuations. A change in the algorithms or conditions would require retuning. The total efficiency average and variance are calculated through expectation value and variance of the weighted mean of each MCCV sample performance using Eq. 20.

$$\begin{aligned} \mathbb{E}[\varepsilon_{\text{total}}] &= \mathbb{E}\left[\frac{\sum_i \omega_i \varepsilon_{ij}}{\sum_i \omega_i}\right] \\ \sigma_{\varepsilon_{\text{total}}}^2 &= \text{Var}\left(\frac{\sum_i \omega_i \varepsilon_{ij}}{\sum_i \omega_i}\right) \end{aligned} \quad (22)$$

where $\varepsilon_{\text{total}}$ is the total efficiency across all IEta bins, ε_{ij} denotes the efficiency of a specific MCCV sample efficiency in a specific IEta bin, j denotes the specific Monte Carlo sample of efficiencies and i denotes the efficiency of a specific IEta bin within the sample.

3.5 Results

3.5.1 Isolation Correlation

Fig. 15 shows the distribution of background events and signal photon events with respect to the isolation variables. The events are binned by their 8-bit isolation coefficient. Bins have been merged such that there are 64 bins for each isolation coefficient, reducing the overall bins along an axis by a factor of 4. The 255 bit coefficient bin for every isolation variable has been set to zero as $\sim 50\%$ of the data for both signal and background was contained in this bin. The tuning will be influenced by the distribution in the rest of the isolation coefficient space. The distributions are combined across all IEta bins.

Fig. 15 generally shows the signal distribution shifted towards higher isolation values compared to the background distribution. Fig. 15a shows a higher density of signal events above 100 in REta and above 250 in RHadV2. Fig. 15d shows a background event cluster below 50 in both RHadV2 and REta. There is also a cluster at REta < 50 and RHadV2 > 250.

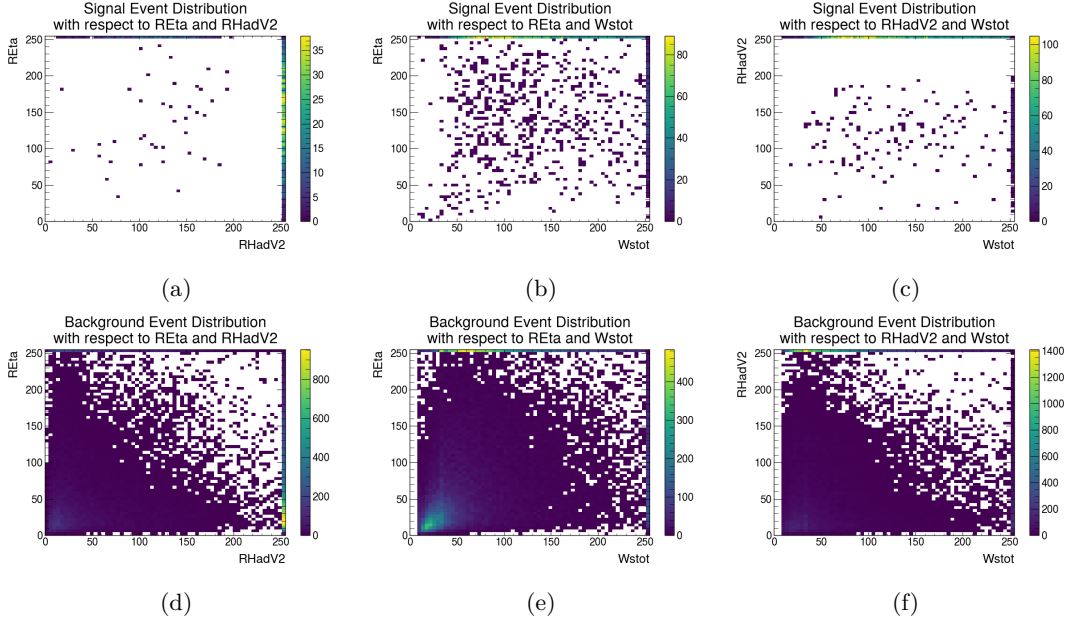


Figure 15: 2D projections of the distribution of photons within the RHadV2, REta and Wstot parameter space. white areas show bins/ areas with no photons. The top right bin (255,255) in either variable has been set to zero so finer correlations can be seen, as this bin contained about 50% of the photons. Each histogram has had bins merged in 4x4 blocks for better visualisation.

Fig. 15b shows a signal event cluster for $REta > 250$ and $50 < Wstot < 200$. The signal distribution has a higher population in the centre of the space ($REta < 250$, $Wstot < 250$) compared to the distributions with respect other variables. Fig. 15e shows a background event cluster in the region $REta > 250$ and $50 < Wstot < 150$, overlapping with the signal event distribution, across all η . There is a second cluster in the range $REta < 70$ and $Wstot < 60$. Fig. 15c shows a signal event cluster in the region $RHadV2 > 250$ and $Wstot > 50$. Fig. 15f shows a background event cluster in the region $Wstot < 100$ and $RHadV2 > 250$. Using the fact that the signal distribution appears to have events clusters at higher isolation coefficients compared to the background it is instructive to construct the optimisation using Eq. 14.

3.5.2 Isolation Tune Performance Measurement

Signal selection efficiency and trigger rate were measured as a total across all η bins using Eq. 20 and Eq. 21 for the Medium isolation parameters. Table 4 shows the energy ranges and the measurements made for the current parameters. The signal selection efficiency can be taken to follow binomial statistics as discussed in section 2.1.

Photon p_t Range/GeV	Cluster Energy Range/GeV	Signal Selection Efficiency/%	Single Trigger Rate/kHz	Diphoton Trigger Rate/kHz
$15 < p_t < 25$	$15 < E_t < 60$	$94.1^{+0.2}_{-0.3}$	107 ± 0.6	1.56 ± 0.1

Table 4: Performance measurements for the previous Medium isolation threshold

A direct rate match between the new isolation parameters and the previous Medium isolation parameters is difficult analytically. A range of target signal selection efficiencies surrounding the measured Medium isolation signal selection efficiency were used to tune new isolation parameters. Rate estimates for each target signal selection efficiency were calculated using the set of new isolation parameters and Eq.21. The estimated rates for each target signal selection efficiency were fit with a cubic polynomial. The target efficiency at which the polynomial equalled the Medium isolation rate was used as the overall signal selection efficiency target.

Fig. 16 shows the trigger rate estimate of applying the new tuning algorithm to the sample of photons. The green horizontal line and confidence interval show the rate of the currently used Medium isolation trigger. The plot highlights that above a 96% target efficiency the rate begins to increase non linearly.

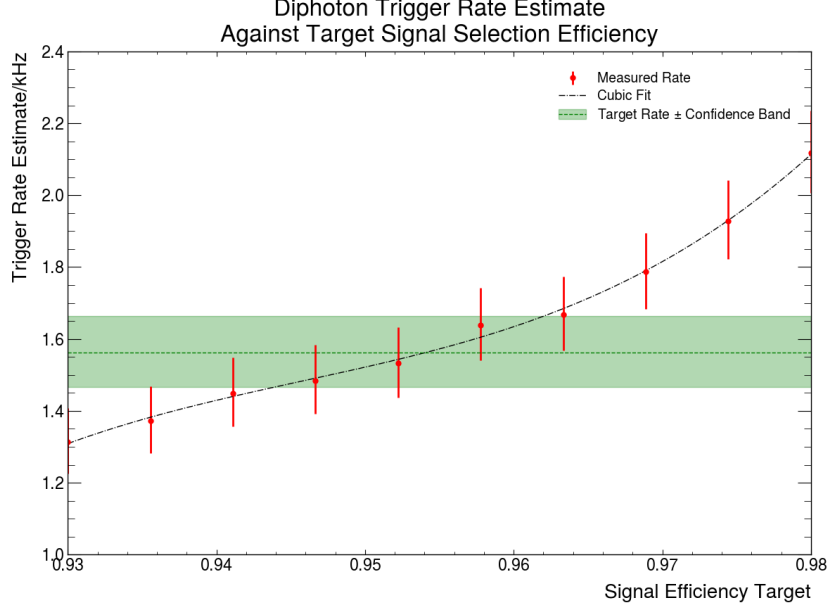


Figure 16: Plot showing the previous menu rate estimate $\pm 1\sigma$ confidence interval (green) and the estimated rate, y axis, after tuning to a specific signal efficiency target, x axis. The fitted cubic equation interpolates the intercept between the data and the previous menu rate.

The intercept of the fitted cubic polynomial gave a target signal selection efficiency of 95.4%. With the target efficiency chosen the minimisation problem can be written:

$$\begin{aligned} & \underset{\vec{x}}{\text{minimize}} && E_{\text{background}}(\vec{x}) \\ & \text{subject to} && E_{\text{signal}}(\vec{x}) \geq 95.4\% \end{aligned} \quad (23)$$

Where \vec{x} denotes the vector of isolation variable coefficients, $E_{\text{background}}$ denotes the background selection efficiency for a specific set of isolation cuts and E_{signal} denotes the signal selection efficiency for a specific set of isolation cuts. A minimisation is computed for each IEta bin within the calorimeter.

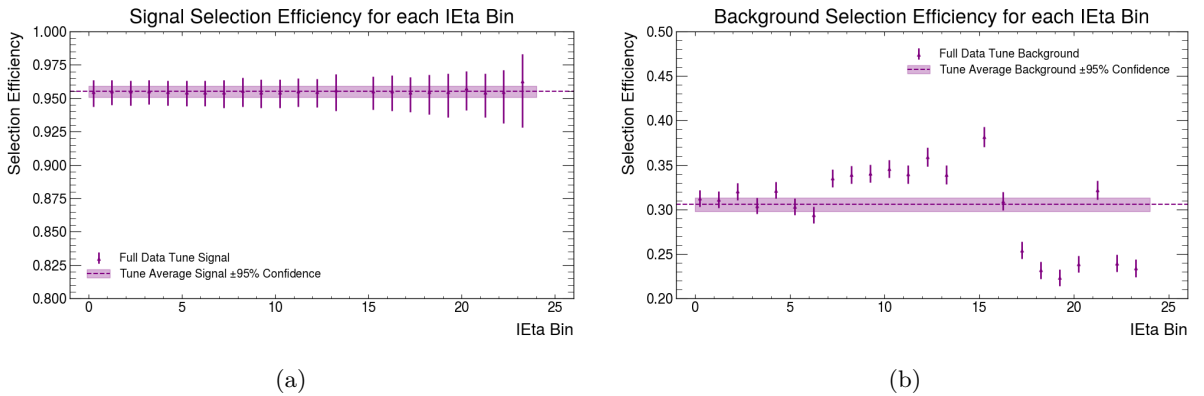


Figure 17: Performance measurements showing the signal (a) and background (b) selection efficiencies, y axes, in IEta, x axis. Performance drawn from the summed volume tables used for tuning. The uncertainties show 68.3%(1 σ) confidence intervals. The horizontal dash axis line shows the total average selection efficiency for signal (a) and background (b). Uncertainty are 95%(2 σ) Clopper-Pearson confidence intervals.

Fig. 17 shows the performance in IEta of the tuning algorithm. Efficiency errors are estimated using 68.3%(1 σ) Clopper-Pearson confidence intervals. The total signal and background efficiencies are estimated by dividing the events passing the isolation cuts in each IEta bin, summed across all

η bins, by the total number of events. Uncertainties are calculated using Clopper-Pearson confidence intervals. The results showed an average signal and background selection efficiency of $(95.5 \pm 0.2)\%$ and $(30.6 \pm 0.2)\%$ respectively, alongside a rate of $(1.55 \pm 0.2)\text{kHz}$. The asymmetry of the errors was negligible to 1 significant figure. The 14th and 24th IEta bins show no data, they are both excluded in the event selection, Section 1.8. The 14th bin covers the transition region and the 24th bin electronics is usually turned off. Both only require no large rate increases in these regions, as they are generally excluded from analysis. This result is outperforming the efficiency of the previous Medium isolation to more than 2σ binomial errors. The new algorithm improves the efficiency on this sample of photons by $\approx 1\%$ whilst maintaining the same rate, to within 1σ .

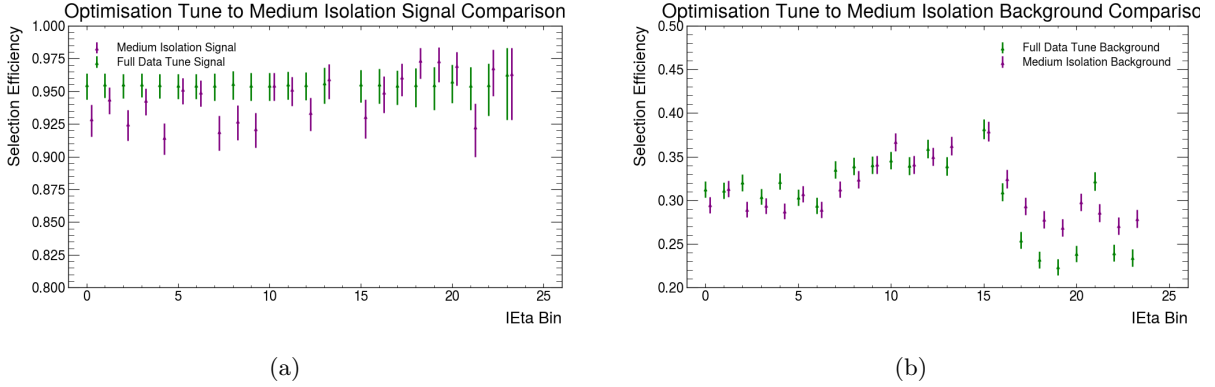


Figure 18: Comparison in the signal (a) and background (b) selection efficiency in IEta between the previous Medium isolation parameters and the parameters chosen by the new implemented algorithm. The uncertainties are generated using 68.3%(1 σ) Clopper-Pearson confidence intervals.

Fig. 18 shows a comparison between the signal selection efficiency of the optimisation algorithm to the currently used Medium isolation criteria. The optimisation has flattened the efficiency across each IEta bin. For the signal selection efficiency, the lower IEta regions increased whilst the higher IEta bins IEta > 17 the efficiency has been lowered making the efficiency equal across η . Fig. 18b shows the background selection efficiency comparison, whilst the lower regions show an increase, the higher regions show a decrease in efficiency. The algorithm balances the signal and background across η targeting a uniform signal selection efficiency.

3.5.3 Isolation Tuning Performance Cross Validation

Whilst the result of sec. 3.5.2 showed an improvement for the algorithm on the sample set of photons. This shows simply that the model can function given a set of photons and criteria to tune to. The result of the tuning algorithm is biased as the optimisation algorithm is performed on the same set of photons that are used to test the model. As such in order to explore the stability of the model, the sufficiency of the data to represent the probability distribution of both background and signal events, and the possible generalisation of the model to unseen data a Monte Carlo cross validation method, randomly dividing the signal and background into a test and training dataset, is implemented. The exact procedure is discussed in section 3.4.

Fig. 19 shows the results of a Monte Carlo Cross validation test compared to the result of the full sample tune, a full sample tune is the new tuning algorithm applied to all 9449 photons and 55325 background events. The Cross validation ran 60 tests per IEta bin, splitting the signal and backgrounds individually into 80% training data and 20% test data. The result shows a drop in signal selection efficiency of $\approx 1\%$ to the full sample tune efficiency. The average total signal selection efficiency was measured at $(94.2 \pm 0.6)\%$ using eq. 22. Fig. 19a shows the variation of the efficiency in higher IEta bins is increased compared to the lower IEta regions near the centre of the detector. The efficiency in these regions drops to 85% at the lowest point, to within 1σ . The average signal selection efficiency variation within each IEta bin was up to 5%, much more than the full sample tune with binomial uncertainties.

The full sample tune signal selection efficiency and the MCCV total signal selection efficiency are consistent within 2σ . However, the significantly larger variation in the MCCV test results indicates instability in the tuning, suggesting the tune is overfitting and optimal parameters are sensitive to the specific data sample. The background selection efficiency exhibits less variation than the signal. Across

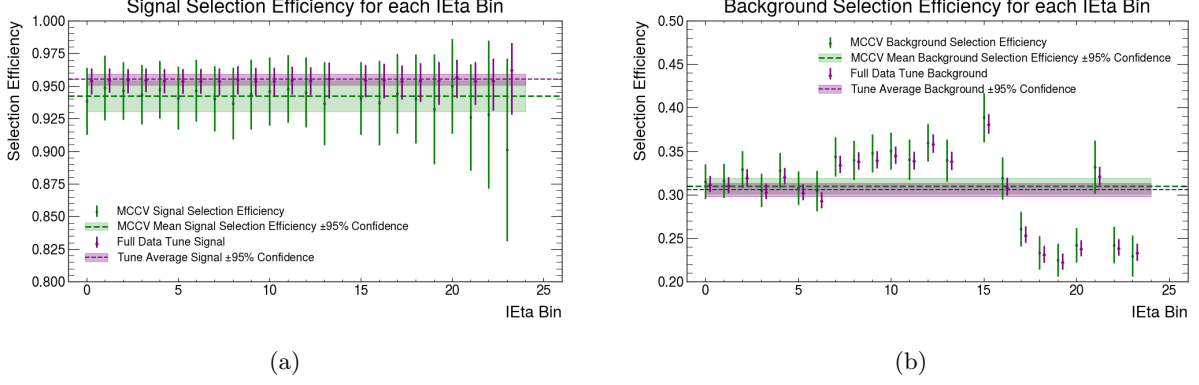


Figure 19: Comparison of selection efficiency for signal (a) and background (b) measured using the Monte Carlo cross validation method and as measured directly from the full data sample (also used to tune). The purple dashed horizontal line shows the average efficiency with 95%(2 σ) Clopper-Pearson uncertainties. The green dashed horizontal line shows the average efficiency from the 60 Monte Carlo samples with 95%(2 σ) Gaussian uncertainty. Bins 14 and 24 have no photon signal data and are omitted from the performance measurements.

all η bins, the average background selection efficiency agrees with the full sample tune to within 1 σ , with a measured value of $(31.0 \pm 0.4)\%$.

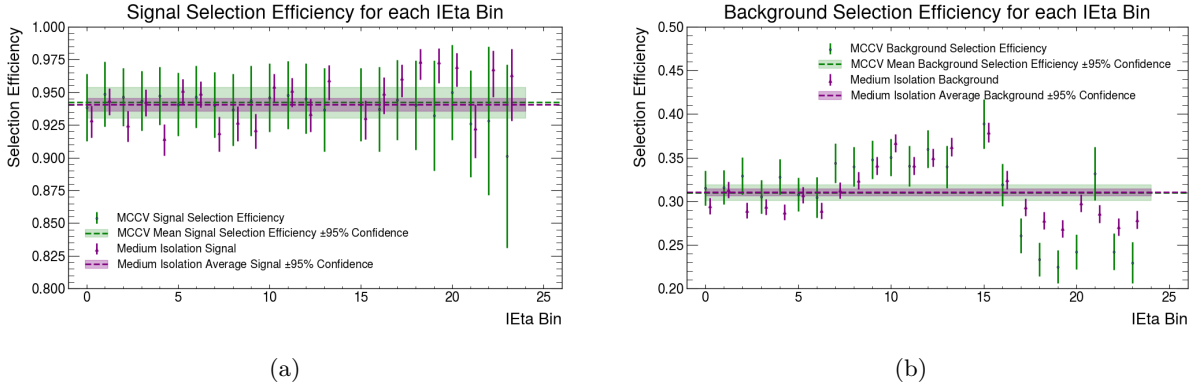


Figure 20: Comparison in selection efficiency between the Monte Carlo generated samples generated from the cross validation for signal selection efficiency(a) and background selection efficiency(b) and the previous Medium isolation performance. The Medium isolation performance data points (purple) have 68.3%(1 σ) Clopper-Pearson confidence intervals. The purple dashed horizontal line shows the average efficiency with a 95%(2 σ) Clopper-Pearson confidence interval. The cross validation measurements (green) have 68.3%(1 σ) Gaussian uncertainties. The green dashed horizontal line shows the average efficiency from the 60 Monte Carlo samples with 95%(2 σ) Gaussian uncertainty. Bins 14 and 24 have no photon signal data and are omitted from the performance measurements.

Fig. 20 shows the comparison of the MCCV performance of the algorithm compared to the Medium isolation criteria. Comparison shows the optimisation algorithm has managed to match the event weighted average background selection efficiency to within 1 σ , $(31.0 \pm 0.4)\%$ MCCV versus $(31.0 \pm 0.2)\%$ Medium isolation. The event weighted signal selection efficiency shows only a minimal increase compared to the currently used Medium isolation criteria. To within 1 σ , $(94.2 \pm 0.6)\%$ MCCV vs $(94.1^{+0.3}_{-0.2})\%$ Medium isolation, the event weighted average is the same as the currently used Medium isolation criteria.

3.5.4 Isolation Tuning Parameter Cross Validation

Fig. 21a shows a comparison between the previously used Medium isolation parameters and the parameters chosen by the new algorithm. As there is no data to tune on in the 14th the isolation parameters have been chosen to the same as the previous Medium isolation parameters. The 24th IEta bin has been chosen to have the same parameters as the 23rd IEta bin. The result can give insight into the difference

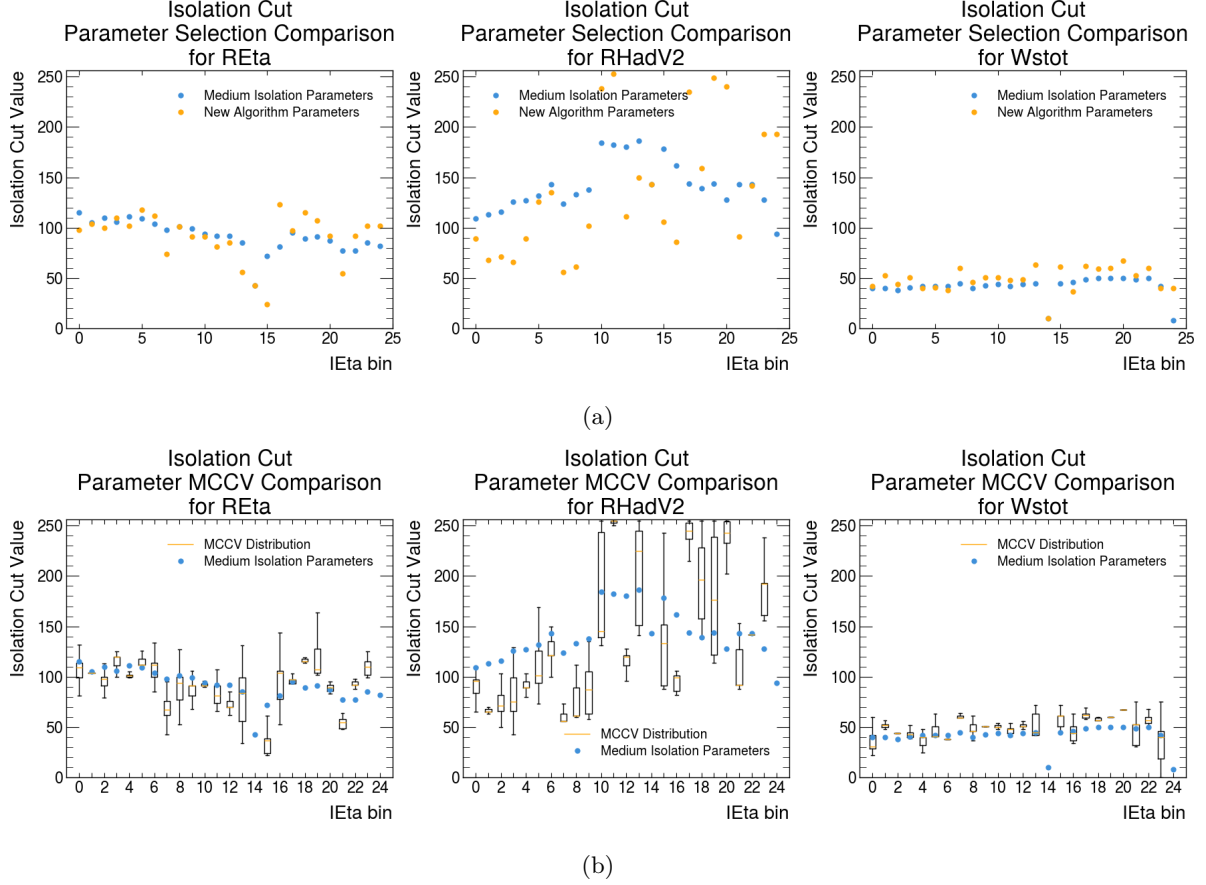


Figure 21: Comparison between isolation variable thresholds, (a) The optimal parameters from the full sample are compared against Medium isolation parameters. (b) Comparison between the cross validation variation of parameters to the Medium isolation parameters. Box plots are used to show the variation with the quartiles highlighted by the edges of the boxes, the whiskers are spaced $1.5\times$ the interquartile range. 50% of the parameters are contained within the range of each box.

between photon and electron distribution with respect to isolation variables.

The new choices show that, in the region $IEta < 10$, the algorithm chose a 10 to 50 integer lower threshold compared to the Medium isolation for RHadV2. REta and Wstot had parameters chosen more similarly to the Medium isolation. This coupled with sections 3.5.2 and 3.5.3 show for $IEta < 10$ a looser set of parameters are possible, whilst maintaining the same background rejection. For the range $10 \leq IEta \leq 15$, the choice of parameters show a possible looser cut on the REta isolation variable and tighter cuts on the Wstot variable. The RHadV2 coefficient shows a tighter cut for $IEta = 10, 11$ and looser cuts for $IEta = (12, 13, 15)$. Apart from $IEta = 21$, for $IEta > 15$ the choices of parameters chosen are tighter than for the previously used parameter choices, this is highlighted by Fig.18 where the signal selection efficiency is similar to the Medium isolation performance, however the background selection efficiency is reduced compared to the Medium isolation background selection efficiency.

Fig. 21b compares the Medium isolation parameters to the variation of the parameters from cross validation of the new tuning algorithm. Box plots are used to show the median and the quartiles of the cross validation sample parameters. The quartiles show the asymmetric spread of the isolation parameters in each IEta bin. The currently used parameters can be considered feasible solutions if the cross validation parameter spread encompasses these values. The discussion considers the spread in the barrel $IEta < 14$ and the inner end cap $IEta > 14$, excluding the transition region.

RHadV2 showed the most variation from the MCCV testing. For $IEta < 14$, the average IQR was 28.3, a $\sim 11\%$ coverage of the RHadV2 space, with a maximum of 105.3, a $\sim 41\%$ coverage of the space. For $IEta > 14$, the average IQR was 40.9, a coverage of $\sim 16\%$, with a maximum of 115.3, a coverage of $\sim 45\%$ of the space. Considering a 95% parameter spread, 11 of the 22 possible IEta tuning bins

had a parameter spread that included the previous Medium isolation parameters. The new algorithm is showing, to 2σ , a possible different optimal set of parameters for 46% of the IEta bins.

REta showed the second most variation in the parameters. For IEta < 14, the average IQR was 12.9, a 5% coverage of the REta space, with a maximum of 50, a $\sim 20\%$ coverage of the space. For IEta > 14, the average spread was 14, a coverage of $\sim 6\%$, with a maximum of 45, a coverage of $\sim 18\%$ of the space. Considering a 95% parameter spread, 12 of the 22 possible tuning parameters from the Medium isolation are contained within the variation of the REta parameters from the cross validation. The new algorithm is showing, to 2σ , a possible different optimal set of parameters for 42% of the IEta bins.

Wstot showed the smallest variation in the parameters chosen by cross validation. For IEta < 14, the average IQR was 5.2, a $\sim 2\%$ coverage of the Wstot space, with a maximum of 21, a $\sim 8\%$ coverage of the space. For IEta > 14, the average spread was 8.5, a coverage of $\sim 3\%$, with a maximum of 28, a coverage of $\sim 11\%$ of the space. considering a 95% parameter spread, 11 of the 22 IEta bins had a parameter variation that coincided with the previous Medium isolation parameters. The new algorithm is showing, to 2σ , a possible different optimal set of parameters for 46% of the IEta bins.

In summary, the REta and Wstot distributions are more clustered in small regions of the parameter space and RHadV2 is less constrained. The new algorithm has found improved parameters for the isolation variables for just under half of all the parameters to 95% confidence intervals.

3.5.5 New Algorithm Efficiency Curve

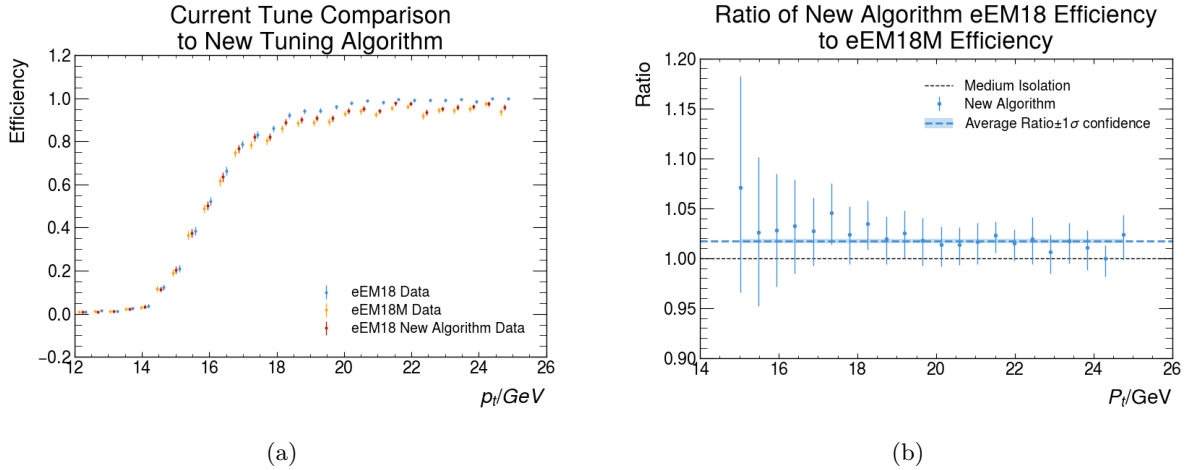


Figure 22: (a) Efficiency plot comparison between the unisolated eEM18 trigger (blue), eEM18M and the eEM18 curve generated using the new set of REta, RHadV2 and Wstot isolation parameters chosen by the new optimisation algorithm. Errors are 1σ Clopper-Pearson confidence intervals. (b) Ratio between the efficiency of the new isolation parameters and the previous Medium isolation parameters in transverse momenta. Errors are 1σ confidence intervals from the combined 1σ confidence intervals of both the Medium isolation and new algorithm isolation. The black dashed horizontal line shows where the Medium isolation level is. Ratio average is error weighted using the average of the asymmetric errors. The ratio average uncertainty is a 1σ Gaussian uncertainty.

Fig. 22 shows the eEM18 efficiency curve, comparing the unisolated trigger, the current Medium isolation trigger and a trigger implemented with the new algorithm parameters. The number of bins are chosen to be $\sqrt{N}/4$, where N is the number of photons in the p_t range $12\text{GeV} \leq p_t \leq 25\text{GeV}$. Each of the different trigger data points have been slightly offset to improve comparison. From fig. 22a, the new algorithm efficiency, red, has been improved compared to the previous Medium isolation, orange. Fig. 22b shows the ratio between the new algorithm efficiency and the previous menu efficiency. The errors on the new algorithm ratio have been propagated such that the Medium isolation ratio can be fixed at 1. The ratio has been measured for photon $p_t > 15\text{GeV}$ as that is the region of interest for improvement. The average ratio is calculated at 1.017 ± 0.002 which shows an average 1.7% increase in the trigger efficiency using the new algorithm parameters. The errors are due to the finite nature of the sample and most ratios are consistent with (but generally all lie above) the Medium isolation to 1σ .

Fig. 23 shows the same comparison as Fig. 22 however, the number of bins has been reduced by a

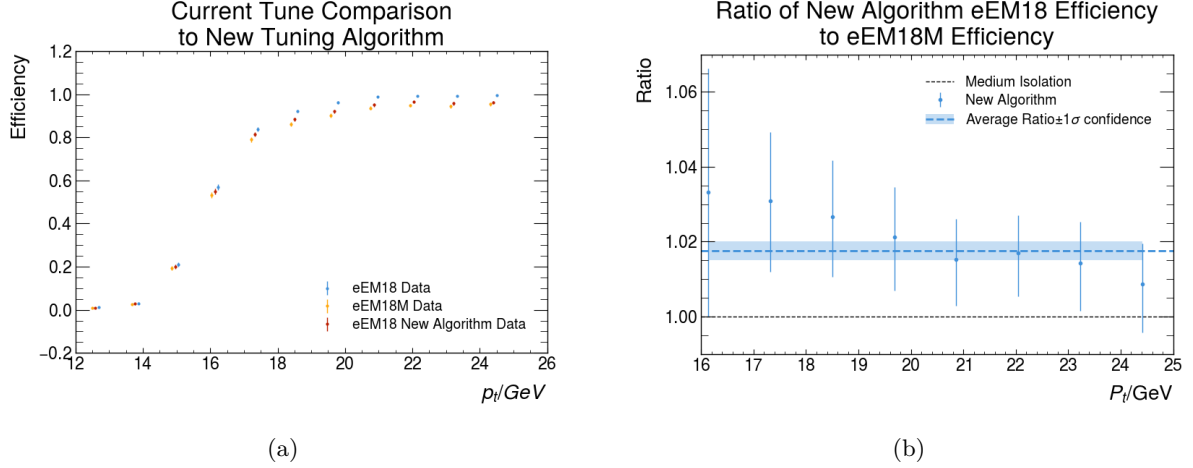


Figure 23: (a) Efficiency plot comparison between the unisolated eEM18 trigger (blue), eEM18M and the eEM18 curve generated using the new set of REta, RHadV2 and Wstot isolation parameters chosen by the new optimisation algorithm. Errors are 1σ Clopper-Pearson confidence intervals. (b) Ratio between the efficiency of the new isolation parameters and the previous Medium isolation parameters in transverse momenta. Errors are 1σ confidence intervals from the combined 1σ confidence intervals of both the Medium isolation and new algorithm isolation. The black dashed horizontal line shows where the Medium isolation level is. Ratio average is error weighted using the average of the asymmetric errors. The ratio average uncertainty is a 1σ Gaussian uncertainty. The bins have been reduced by a factor of 2 to increase statistics available.

factor of 2. The reduction in bins increases the per bin statistics and improves the comparison between the previous Medium isolation and the new algorithm parameters' performance. The increased statistics show an increased performance of the new algorithm parameters, the ratio lies more than 1σ from the current Medium isolation for the bins excluding the first two and last one in fig. 23b. The key region when the trigger is reaching 90% selection efficiency, $\sim 19\text{GeV}$, is increased (to more than 1σ) compared to the Medium isolation selection efficiency.

4 Discussion

4.1 Efficiency Performance Measurements

The efficiency curves for the main L1 triggers used in physics analysis have been generated and analysed. Data had been re-simulated to include the new 2025 RHadV2 isolation definition. The triggers all surpass 95% efficiency and asymptote to close to 100%, Fig.9. The Monte Carlo purity analysis, Section 2.2.1, showed good purity for photons above $\sim 15\text{GeV}$. The Monte Carlo sample overestimated the data photon distribution which could be due to the limited sample size, 4946 photons from Monte Carlo and 51356 from data. This could also be caused by the inability to estimate the fake rate, other objects reconstructed as photons, using Monte Carlo.

The variation of trigger performance with pileup and η was measured, sections 2.2.3 & 2.2.4. To 2σ all the triggers have a uniform performance in both η and μ . The offline photon p_t at 90% trigger efficiency is used as a comparable measure between efficiency curves with an increased photon p_t at 90% trigger efficiency indicating worse trigger performance.

The newly introduced computational fitting algorithm, Section 2.1.2, presents a method to measure the performance of hundreds of trigger curves computationally, robustly and rapidly. The new method combined with the offline photon p_t at 90% trigger efficiency as a performance metric allows accurate performance comparisons in pseudorapidity, pileup and across a range of trigger energy thresholds.

The new fitting algorithm uses a fixed $\pm 2\text{GeV}$ fitting window, based on the typical trigger turn on width, 3 to 5GeV. The reduced range focusses the fit on the shape of the specific p_t region, however, the method is not completely robust as the turn-on width varies with trigger energy threshold and location on the efficiency curve, plateau or turn-on. A more flexible method could first calculate the offline photon

p_t difference between the 10% and 90% trigger efficiency levels using the fixed window, then adjust the fitting window to a fraction of this width. Further, a quadratic function could be preferred over a fermi function. Polynomials are more widely used for interpolation and a quadratic fit could approximate coefficients of a second order Taylor expansion.

The results overall show that for the higher p_t photons ($p_t \geq 18\text{GeV}$) and within tolerances, the triggers are all functioning correctly, are unaffected by variation in the measuring conditions within the ATLAS detector and reach a sufficient level of selection efficiency at the energies where offline analysis begins. The triggers below 18GeV are being adversely affected by the isolation criteria and have scope to be improved.

4.2 Isolation Tuning Algorithm

The proposed new tuning algorithm was matched to the rate of the previously used set of Medium isolation parameter cuts. The rate of the optimised set of parameters was measured at $(1.55 \pm 0.1)\text{kHz}$ for the new set of parameters and the currently used set of Medium isolation cuts had a rate of $(1.56 \pm 0.1)\text{kHz}$. For the given sample of photons the algorithm found a more optimal set of cuts that improved the signal selection efficiency by $\approx 1\%$ when averaged across all IEta bins. The algorithm also flattened the signal selection efficiency to target the same signal selection efficiency within each IEta bin.

The optimisation algorithm was tested for stability, overfitting and data insufficiency by employing a new Monte Carlo cross validation method, Section 3.5.3. The MCCV results showed that the unbiased signal selection efficiency decreased and only minimally outperformed the currently used Medium isolation parameters. The average total efficiency across all IEta bins was measured at $(94.2 \pm 0.6)\%$ using the Monte Carlo generated samples. The previous Medium isolation had a signal selection efficiency of $(94.1^{+0.2}_{-0.3})\%$ on the sample of photons. The 23rd IEta bin had the most variation of signal selection efficiency, with a 1σ variation of 6.4%. Each IEta bin on average had a 3.1% 1σ variation in signal selection efficiency.

The background selection efficiency could still match the performance of the previous Medium isolation parameters to within 1σ . $(31.0 \pm 0.4)\%$ for the MC samples and $(31.0 \pm 0.4)\%$ for the Medium isolation selection. The average 1σ variation in background selection efficiency of each IEta bin using the MC samples was measured at 2.1%, with a maximum 1σ variation of 2.9% in the 15th IEta bin. Variance of the average total background selection efficiency was smaller than for the signal selection efficiency $\pm 0.4\%$ versus $\pm 0.6\%$.

The Monte Carlo spread of the performance does not include the binomial statistics that would apply to each of the generated Monte Carlo samples. Accounting for the binomial statistics of each sample would create asymmetric errors on the MC distribution, the confidence interval would also become wider. The binomial statistics are highlighted by the spread on the full dataset tune, fig. 17. The additional effects of binomial statistics are assumed not to influence the results sufficiently for a full calculation and would decrease with an increased sample size.

Section 3.5.4 showed that the RHadV2 isolation parameter was most susceptible to input data variations. Cross validation showed that 50% of parameters spanned 45% of the RHadV2 subspace in the worst performing IEta bin. The average variation spanned $\sim 11\%$ and $\sim 16\%$ of the subspace for the barrel, IEta < 14 , and end cap, IEta > 14 , respectively. Fig. 15a showed a sparse RHadV2 distribution for RHadV2 < 250 . REta and Wtot had a higher distribution below 250. Hence, this leads to the larger fluctuations compared to the other parameters.

The algorithm uses a brute force search. The optimal parameters are chosen from the total set of all parameter combinations given the selection efficiencies for signal and background. The algorithm will naturally over fit to the given sample and therefore assumes that the sample adequately represents the true distribution, with respect to the isolation variables, of photon and background events in each IEta bin. The total number of photons in the sample was 9449. The optimisation space has 16.7 million possible parameter combinations per IEta bin of 25 total IEta bins, so each space was sparsely populated. From Section 3.3, the distribution of photons decreases with increasing IEta and the 23rd IEta bin contained only 81 photons. This leads to the increased variation in the cross validation tests.

The tuning currently treats parameters independently, cuts are made on each parameter separately. Hence, it is not necessary to have enough data to fill the total optimisation space. It is sufficient to have data to represent each parameter distribution independently. Considering a Poisson distribution, the

relative error on each bin is $\frac{1}{\sqrt{N_i}}$, with N_i the population of each bin. For a 10% relative bin population error and considering a uniform distribution of events across each isolation parameter, the total number of events required would be approx. 25600 events per IEta bin, 100 events per isolation parameter bin and 256 bins. With 25 IEta bins and approx. 0.8% of events in the 23rd IEta bin, an upper limit of ≈ 3.2 million total events would be required. Given 9449 events were drawn from 12.2fb^{-1} , 4000fb^{-1} of ATLAS data would be required to adequately fill the optimisation space, far exceeding the data available from ATLAS. There are a few options to overcome this data limitation. One option would be to generate specific Monte Carlo samples for photons or FSR events. Whilst this would generate more events, Monte Carlo cannot completely capture the fine details of the calorimeter, so for tuning purposes it is better to use a data sample. This could be achieved by using a different event selection with a higher cross section and less strict dependency on a specific decay. Alternatively, if the difference in photon and electron distributions are considered negligible (as is currently assumed at L1), a sample of electrons from $Z \rightarrow e^+e^-$ decays could be tuned at lower energies.

The proposed new algorithm presents a more robust, accurate and flexible way to tune the trigger isolation parameters. The tune can target trigger rates or selection efficiencies for signal and background within each IEta bin or across all IEta bins. Cross validation of the results ensures robust, optimal solutions less sensitive to statistical fluctuations. Further, the algorithm could be used to computationally explore Pareto optimal solutions, which balance the effect on all cost functions in multi objective optimisations. Summed volume tables can also calculate the sum of sub regions with $O(1)$ complexity[36]. Hence, optimisation including subregions of the optimisation space could be ran. Section 3.5.1 showed a higher density of background events in the central region of the isolation coefficient space compared to photons. Performance could be improved by allowing subspace cuts on these regions.

5 Conclusion

The project aimed to measure and improve the performance of the photon triggers used in the ATLAS detector. Performance is measured by a close agreement between an unisolated and isolated trigger. The offline photon p_t at 90% trigger efficiency ($E_{90\%}$) was used to measure the uniformity of performance in pseudorapidity and pileup. Section 2 presented the measurements made on the eEM18M, eEM24L and eEM26M triggers used within ATLAS. The measurements included the new definition of isolation adopted in 2025. Monte Carlo purity analysis showed good rejection of coincident photons for the event selection in the p_t range required to make photon measurements, reaching a 95% purity at $(15.4 \pm 1.1)\text{GeV}$ however this was not an exhaustive method; failing to consider fake identification rates.

The eEM26M, eEM24L and eEM18M all showed efficiency curves starting at zero and rising to near 100% efficiency 3 to 5GeV from the trigger energy threshold and 90% photon identification efficiencies at $(27.8 \pm 0.1)\text{GeV}$, $(25.1 \pm 0.1)\text{GeV}$ and $(19.1 \pm 0.6)\text{GeV}$ respectively. For physics analysis: the eEM26M will be above 99% efficient at 140GeV. The eEM24L trigger will be 90% efficient at 25GeV and above 97% efficient at 35GeV. The eEM18M trigger will be above 90% efficient at 20GeV and will be nearing 95% efficiency at 22GeV. All triggers showed uniformity to within 2σ in η , with a decreased performance compared to the average around the transition region, $1.37 < \eta < 1.52$. Pileup measurements showed uniform performance to 1σ errors for the eEM26M and eEM18M, triggers. The eEM24L performance was uniform to less than 2σ errors. The trigger performance variation with trigger energy threshold showed decreased performance due to isolation below a trigger threshold of 18GeV.

The reduced trigger performance below 18GeV prompted development of an algorithm using summed volume tables to increase signal selection efficiency for low energy triggers. The new algorithm targetted the same rate as the previous Medium isolation and results were compared to this isolation level. The results for a sample of $15 \leq p_t \leq 25\text{GeV}$ photons showed an improved selection efficiency, $(95.5 \pm 0.2)\%$ versus $(94.1^{+0.3}_{-0.2})\%$, and consistent rate, $(1.55 \pm 0.1)\text{kHz}$ versus (1.56 ± 0.1) , compared to the previous Medium isolation. An efficiency curve generated using the new isolation parameters showed an average 1.8% increase in trigger efficiency across the photon p_t range, $16 \leq p_t \leq 25\text{GeV}$. Individual bin efficiencies were increased to more than 1σ compared to the previous Medium isolation.

Cross validation showed that the algorithm would over fit to the given optimisation sample and the data was insufficient to represent the true distribution of photons with respect to the isolation variables. Results showed a decrease in signal selection efficiency, $(94.2 \pm 0.6)\%$ versus $(94.1^{+0.3}_{-0.2})\%$ and a consistent background selection efficiency, $(31.0 \pm 0.4)\%$ versus $(31.0 \pm 0.2)\%$, compared to the previous Medium isolation. A conservative 3.2 million photons, compared to the used sample of 9449 photons, in the p_t

range $15 \leq p_t \leq 25\text{GeV}$ would be needed to have an uncertainty of 10% in each isolation variable bin for each IEta region. Cross validation also considered the spread of the optimisation parameters. Of the 25 possible IEta bins, 5 had all three Medium isolation parameters and 19 had at least one parameter lie within the 95% spread of the cross validation parameters.

References

- [1] The ATLAS Collaboration. Observation of a new particle in the search for the standard model higgs boson with the atlas detector at the lhc. *Physics Letters B*, 716(1):1–29, September 2012.
- [2] Edward Scott. Measurements of the Higgs boson decaying into two photons at CMS. *PoS, ICHEP2018:260*, 2019.
- [3] The ATLAS Collaboration. The ATLAS experiment at the CERN large hadron collider: a description of the detector configuration for run 3. *Journal of Instrumentation*, 19(05):P05063, May 2024.
- [4] G Apollinari, O Brüning, T Nakamoto, and L Rossi. High luminosity large hadron collider hl-lhc, 2015.
- [5] The ATLAS Collaboration. Electron efficiency measurements with the ATLAS detector using 2012 lhc proton–proton collision data. *The European Physical Journal C*, 77(3), March 2017.
- [6] The ATLAS Collaboration. Performance of electron and photon triggers in ATLAS during LHC run 2. *The European Physical Journal C*, 80(1), January 2020.
- [7] The ATLAS Collaboration. The atlas trigger system for lhc run 3 and trigger performance in 2022. *Journal of Instrumentation*, 19(06):P06029, June 2024.
- [8] The ATLAS Collaboration. The atlas experiment at the cern large hadron collider. *Journal of Instrumentation*, 3(08):S08003, aug 2008.
- [9] The ATLAS Collaboration. ATLAS Liquid Argon Calorimeter Phase-II Upgrade: Technical Design Report. Technical report, CERN, Geneva, 2017.
- [10] The ATLAS Collaboration. Electron and photon performance measurements with the ATLAS detector using the 2015-2017 LHC proton-proton collision data. *JINST*, 14(12):P12006, 2019. 31 figures, 3 tables. All figures including auxiliary figures are available at <https://atlas.web.cern.ch/Atlas/GROUPS/PHYSICS/PAPERS/EGAM-2018-01>.
- [11] M (CERN) Aleksa, W (Pittsburgh) Cleland, Y (Tokyo) Enari, M (Victoria) Fincke-Keeler, L (CERN) Hervas, F (BNL) Lanni, S (Oregon) Majewski, C (Victoria) Marino, and I (LAPP) Wingerter-Seez. ATLAS Liquid Argon Calorimeter Phase-I Upgrade: Technical Design Report. Technical report, CERN, 2013. Final version presented to December 2013 LHCC.
- [12] The ATLAS Collaboration. *ATLAS level-1 trigger: Technical Design Report*. Technical design report. ATLAS. CERN, Geneva, 1998.
- [13] The ATLAS Collaboration. Performance of the ATLAS Track Reconstruction Algorithms in Dense Environments in LHC run 2. *Eur. Phys. J. C*, 77(10):673, 2017. 44 pages in total, author list starting page 28, 17 figures, 1 table, submitted to EPJC, All figures including auxiliary figures are available at <http://atlas.web.cern.ch/Atlas/GROUPS/PHYSICS/PAPERS/PERF-2015-08/>.
- [14] The ATLAS Collaboration. Jet reconstruction and performance using particle flow with the atlas detector. *The European Physical Journal C*, 77(7), July 2017.
- [15] Christian Wolfgang Fabjan and F Gianotti. Calorimetry for Particle Physics. *Rev. Mod. Phys.*, 75:1243–1286, 2003.
- [16] C. W. Fabjan and D. Fournier. *Calorimetry*, pages 201–280. Springer International Publishing, Cham, 2020.
- [17] Alexander Belyaev and Douglas Ross. *Particle Detectors*, pages 221–230. Springer International Publishing, Cham, 2021.
- [18] Francesca Cavallari. Performance of calorimeters at the lhc. *Journal of Physics: Conference Series*, 293(1):012001, apr 2011.

- [19] The ATLAS collaboration. *ATLAS calorimeter performance: Technical Design Report*. Technical design report. ATLAS. CERN, Geneva, 1996.
- [20] Yuji Enari and on behalf of the ATLAS Collaboration. The phase-1 trigger readout electronics upgrade of the atlas liquid argon calorimeter. *Journal of Physics: Conference Series*, 1162(1):012041, jan 2019.
- [21] The ATLAS Collaboration. Search for boosted low-mass resonances decaying into hadrons produced in association with a photon in pp collisions at $\sqrt{s}=13$ TeV with the ATLAS detector, 2024.
- [22] The ATLAS Collaboration. Measurement of the higgs boson mass with $H \rightarrow \gamma\gamma$ decays in 140 fb⁻¹ of $\sqrt{s} = 13$ TeV pp collisions with the ATLAS detector. *Physics Letters B*, 847:138315, December 2023.
- [23] The ATLAS Collaboration. Search for diphoton resonances in the 66 to 110 gev mass range using pp collisions at $\sqrt{s} = 13$ TeV with the ATLAS detector. *Journal of High Energy Physics*, 2025(1), January 2025.
- [24] The ATLAS Collaboration. Search for boosted diphoton resonances in the 10 to 70 gev mass range using 138 fb¹ of 13 TeV pp collisions with the ATLAS detector. *Journal of High Energy Physics*, 2023(7), july 2023.
- [25] ATLAS Collaboration. MCTruthClassifier, 2021. ATLAS internal TWiki. Restricted Access.
- [26] Paolo Nason. A New method for combining NLO QCD with shower Monte Carlo algorithms. *JHEP*, 11:040, 2004.
- [27] Stefano Frixione, Paolo Nason, and Carlo Oleari. Matching NLO QCD computations with Parton Shower simulations: the POWHEG method. *JHEP*, 11:070, 2007.
- [28] Simone Alioli, Paolo Nason, Carlo Oleari, and Emanuele Re. A general framework for implementing NLO calculations in shower Monte Carlo programs: the POWHEG BOX. *JHEP*, 06:043, 2010.
- [29] Christian Bierlich, Smita Chakraborty, Nishita Desai, Leif Gellersen, Ilkka Helenius, Philip Ilten, Leif Lönnblad, Stephen Mrenna, Stefan Prestel, Christian T. Preuss, Torbjörn Sjöstrand, Peter Skands, Marius Utheim, and Rob Verheyen. A comprehensive guide to the physics and usage of pythia 8.3, 2022.
- [30] Simone Alioli, Paolo Nason, Carlo Oleari, and Emanuele Re. NLO vector-boson production matched with shower in POWHEG. *JHEP*, 07:060, 2008.
- [31] Simone Alioli, Keith Hamilton, Paolo Nason, Carlo Oleari, and Emanuele Re. Jet pair production in POWHEG. *JHEP*, 04:081, 2011.
- [32] D Casadei. Estimating the selection efficiency. *Journal of Instrumentation*, 7(08):P08021–P08021, August 2012.
- [33] Erwin Bolthausen and Mario V. Wüthrich. Bernoulli’s law of large numbers. *ASTIN Bulletin*, 43(2):73 – 79, 2013. Published online Juni 2013. It was possible to publish this article open access thanks to a Swiss National Licence with the publisher.
- [34] Johannes Haase. Study of the electron \rightarrow photon misidentification rate in the ATLAS detector, 2011.
- [35] Christian Reinbold and Rüdiger Westermann. Parameterized splitting of summed volume tables. *Computer Graphics Forum*, 40(3):123–134, 2021.
- [36] Yan Ke, R. Sukthankar, and M. Hebert. Efficient visual event detection using volumetric features. volume 1, pages 166– 173 Vol. 1, 11 2005.
- [37] Franklin C. Crow. Summed-area tables for texture mapping. *SIGGRAPH Comput. Graph.*, 18(3):207–212, January 1984.
- [38] P. Viola and M. Jones. Rapid object detection using a boosted cascade of simple features. In *Proceedings of the 2001 IEEE Computer Society Conference on Computer Vision and Pattern Recognition. CVPR 2001*, volume 1, pages I–I, 2001.
- [39] Abhishek Bansal. 3d variant for summed area table (SAT). <https://stackoverflow.com/questions/20445084/3d-variant-for-summed-area-table-sat>. accessed: Jan-2025.

- [40] Richard Simon. *Resampling Strategies for Model Assessment and Selection*, pages 173–186. 04 2007.